COMPARISON OF RADIATION DAMAGE EFFECTS IN ORGANIC AND SILICON PHOTODETECTORS

A Thesis
Presented to
The Academic Faculty

By

Jacob W. Inman

In Partial Fulfillment
of the Requirements for the Degree
Master of Science in the
School of Nuclear and Radiological Engineering

Georgia Institute of Technology

May 2019

COMPARISON OF RADIATION DAMAGE EFFECTS IN ORGANIC AND SILICON PHOTODETECTORS

Approved by:

Dr. Nolan E. Hertel, Advisor
School of Mechanical Engineering,
Nuclear Engineering Program
Georgia Institute of Technology

Dr. Bernard J. Kippelen
School of Electrical and Computer Engineering
Georgia Institute of Technology

Dr. Chris C-K Wang
School of Mechanical Engineering,
Nuclear Engineering Program
Georgia Institute of Technology

Date Approved: April 24, 2019

ACKNOWLEDGEMENTS

I would first like to thank my thesis advisor, Dr. Nolan Hertel, whose encouragement, support, and deep well of knowledge made the development of this thesis possible. He has been an invaluable resource not only in writing my thesis, but in every aspect of my career as a graduate student. In addition, I want to express my deep gratitude to Dr. Bernard Kippelen and Dr. Chris Wang for their advice and for serving on my thesis reading committee. Special thanks are due to Dr. Canek Fuentes-Hernandez, who has not only spent countless hours working on this project with me, but also has provided me an incredible amount of advice and guidance during our time working together. I would also like to thank the Office of Radiological Safety (specifically, Christina Tabor, Steve Grimm, Gary Spichiger, and Darrell Neal) for helping me set up experiments in the lab; by that same token, I want to thank Colin Thomas and Andrew Conant for helping me tear down the experiments performed in the high bay. I would also like to extend my thanks to Dr. Paul Rose, Xiaojia Jia, and Wen-Fang Chou for their advice and assistance during these experiments, and thank John Stooksbury, Caleigh Samuels, and Greg Szalkowski for providing me invaluable MCNP assistance. Finally, I must thank my family (particularly my sister Deidre, who lent her editing skills to this work) for all of their support and love; this work would not exist without them.

TABLE OF CONTENTS

LIST OF TABLES

LIST OF FIGURES

SUMMARY

Field deployment of radiation detectors for use in nuclear material verification and in portal monitors requires rugged systems capable of withstanding high fluences of mixed-field radiation. As the use of solid-state photodetectors (for use in scintillation light detection) has grown in recent years, their ability to maintain performance under intense irradiation has come into question. This study seeks to determine the amount of radiation damage that both silicon (the current solid-state standard device) and organic photodetectors can withstand while maintaining their performance. Using a high-activity radioactive source, samples were irradiated for several hours and then measured for changes in leakage current with varying bias voltage. In addition, MCNP models were developed for these experiments in order to quantify the level of radiation damage and absorbed dose within each photodetector type. Results indicate that organic photodetectors show high resilience to radiation-induced damage and do not require time to self-anneal in order to return to pre-irradiation performance levels, even under significantly higher dose rates than in silicon. Though silicon devices will self-anneal and recover roughly 50% of performance several hours after irradiation is completed, significant and lasting impacts on leakage current were noted.

CHAPTER 1
INTRODUCTION AND BACKGROUND

1.1 Introduction

The field of radiation detection via scintillation counting, with its diverse and ever-expanding applications, has long relied on the use of photomultiplier tubes (PMTs) in order to convert scintillation light into useful electrical pulses. Providing little in the way of excess noise (of central concern when low-output scintillators can provide only a few hundred or thousand photons per pulse), PMTs are still widely employed in even the most cutting-edge of research with scintillation detectors. However, the drawbacks associated with PMTs, such as the high voltage (ca. 1-3 kV) required for them to achieve the signal amplification needed for each pulse and the fragility of their internal components, have inspired a search for new methods of signal conversion. Silicon photomultipliers (SiPMs) and photodiodes (SiPDs) have largely fulfilled that role, requiring very little in the way of applied bias voltage (ca. 0-30 V) and, as solid-state devices, are much more rugged than the delicate PMTs of the past [1]. Though these devices have since become ubiquitous in research environments, silicon-based detectors have their own drawbacks: the delicate nature of semiconductors in high-flux environments make silicon unattractive when utilizing high-activity sources of radiation [2, 3].

One potential solution to this problem can be found in organic photodetectors (OPDs, specifically organic photodiodes; these terms will be used interchangeably in this work). Rugged, physically flexible, and inexpensive, OPDs operate under similar conditions as SiPDs, with high quantum efficiency [1] and low power requirements (operating voltages of ca. 0-10 V). Most importantly for this work, however, OPDs show promising signs of resistance to radiation damage in high fluence environments. This idea has gone largely

untested, however; as OPDs have not been considered candidates for use in high-energy physics experiments, their resistance to radiation has not been studied as thoroughly. In order to attempt to quantify the level of degradation undergone by OPDs in high-fluence environments, several of these devices were exposed to a high-activity AmBe mixed-field radiation source for varying lengths of time. Measurements of the leakage current (or dark current, the current through the device even in the absence of ionizing radiation) of the device took place both before and after irradiation to attempt to quantify the level of degradation. These results were then compared to results for silicon photodetectors obtained from literature to determine their relative effectiveness. In addition to these physical experiments, computational models were developed to study and validate the γ-ray and neutron dose delivered to each of these photodiode types during irradiation using the Monte Carlo N-Particle transport (MCNP) code. These results allowed for comparison between the assumed experimental dose rate and the theoretical absorbed dose, from which experimentally-derived quantities could be ascertained.

1.2 Background

1.2.1 Radiation Damage in Silicon Photodetectors

Radiation damage in inorganic semiconductors (such as SiPDs) occurs principally via two methods: non-ionizing energy loss in bulk material and ionizing energy loss at the surface of the material. Though ionizing energy loss is typically of more vital concern for nuclear engineers, in this case it is the non-ionizing energy loss in the material that leads to the degradation of a semiconducting detector [2].

Ionizing radiation, such as neutrons or γ-rays, passing through the crystal structure of bulk silicon can create ions along its path via the stripping of electrons. However, this process is reversible, as free electrons are abundant in the lattices of bulk silicon. Damage in the structure of the bulk material occurs when incident radiation collides with silicon atoms in the crystal itself, displacing primary knock-on atoms (PKA) at energies exceeding the

threshold of 25 eV and creating vacancies in the lattice [3]. These defects can then combine with other defects in the structure to create localized, highly disordered regions in the crystal structure. While these effects are typical of radiation damage in inorganic materials of all types, semiconductors are highly susceptible to the creation of defects within the depleted region of the device, or the area in which electron-hole pairs (also known as excitons) combine to create a voltage drop across the semiconductor [1]. Defects in this region cause a divergence in the number of electron donor and acceptor sites within the semiconductor, an effect which directly impacts the depletion voltage (or the voltage required across the detector depth for full charge collection) of the detector:

$$N_{eff} = \frac{2\varepsilon\varepsilon_0}{q_0 d^2} V_{depl}, \tag{1.1}$$

where q_0 is the elementary charge (1.6x10^{-19} C), $\varepsilon\varepsilon_0$ is the permittivity of silicon, d is the detector thickness, V_{depl} is the voltage across the depleted region, and N_{eff} is the effective impurity concentration in the depleted region, defined as the difference in the number of donor sites and the number of acceptor sites [3]. This impurity concentration is directly impacted by the fluence of incoming particles via the following relation:

$$N_{eff}(\phi) = N_{D,0} e^{-c_D \phi} - N_{A,0} e^{-c_A \phi} - b\phi, \tag{1.2}$$

where ϕ is the incoming neutron fluence, $N_{D,0}$ and $N_{A,0}$ are the number of donor and acceptor sites prior to irradiation, respectively, c_D and c_A are the removal rate of donor and acceptor sites during irradiation, respectively, and b is the rate of increase of acceptor sites during irradiation [2]. A consequence of this relationship between fluence and impurity concentration (and, as an extension, the depletion voltage) is that above fluences on the order of 10^{12} $\frac{\text{neutrons}}{\text{cm}^2}$, a sharp increase in impurity concentration arises (see figure 1.1).

As can be seen, there is a clearly defined fluence threshold for impurity production in silicon at 10^{12} $\frac{\text{n}}{\text{cm}^2}$. This minimum suggests an intrinsic semiconductor, or one that has

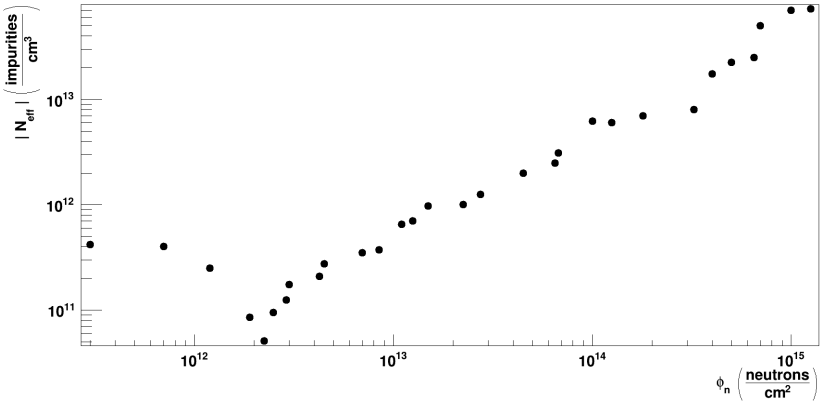

Figure 1.1: Effective impurity concentration as a function of neutron fluence. Data obtained from from [2].

donor and acceptor sites in equilibrium with one another, allowing the depletion voltage to be reduced to nearly zero at that location [2]. At higher fluences, the impurity concentration grows precipitously, an effect that is largely due to an increase in parameter b, the rate of acceptor creation, above fluences of 10^{13} $\frac{\text{n}}{\text{cm}^2}$ [4]. Not coincidentally, depletion voltage also increases significantly at these fluences as the semiconductor gradually changes from its original n-type configuration to a p-type detector as the number of acceptors present outstrip the removed donor sites via a process known as inversion bulk doping [5]. This effect also results in a notable increase in the leakage current [1].

The overall effect of these changes at the detection level is that ever-increasing amounts of bias voltage are required in order to maintain full charge collection in the photodetector and the eventual breakdown of scintillation light conversion in the device is inevitable [6]. In addition to charge collection issues, increases in both the depletion voltage and leakage current require higher power dissipation as well, resulting in silicon self-heating and the potential for thermal runaway and quicker breakdown of the device.

Though the impact of irradiation on the performance of silicon detectors is undeniable, there is a fairly simple method by which these devices can recover from this damage without specialized techniques. This process is known as self-annealing, by which irradiated

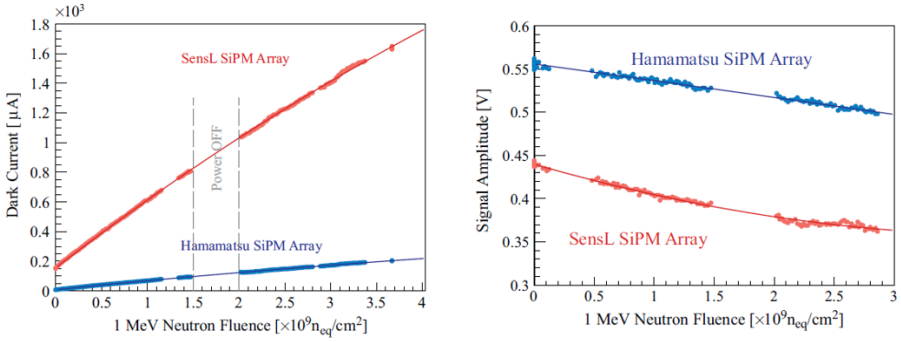

(a) Effect of irradiation on the dark current (left) and depletion voltage (right) of SiPMs.

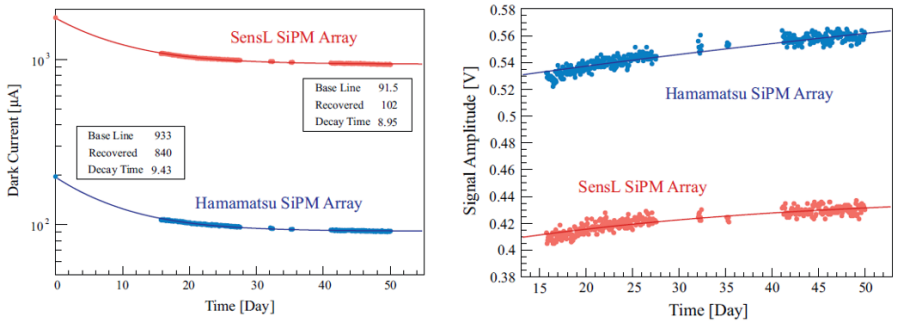

(b) Recovery of dark current (left) and depletion voltage (right) in SiPMs post-irradiation.

Figure 1.2: Recovery of dark current and depletion voltage in SiPMs due to the self-annealing phenomenon. Taken from [7].

samples are left untouched at room temperature for extended periods of time. In order to quantify the impact of self-annealing, samples are analyzed for an extended length of time post-irradiation, measuring both the depletion voltage and dark current of the devices [7]. As is shown in figures 1.2a and 1.2b, both depletion voltage and dark current recover to a great extent by simply allowing the irradiated crystal structure of silicon to relax itself to a new equilibrium. This study found that depletion voltage recovered back to its pre-irradiation level, while dark current recovered from roughly half the damage done via irradiation.

Though these self-annealing effects are displayed for fluences far below our region of interest (10^{12}-10^{15} $\frac{n}{cm^2}$), more recent studies have indicated that recovery occurs even when samples undergo much higher-fluence irradiations [8]. It has since been shown that higher

temperature annealing periods for a short time post-irradiation can increase the speed of recovery as well [3]. In addition, a solution utilizing oxygenation of silicon samples has shown the ability to reduce the impact of radiation damage on impurity concentration and depletion voltage, but, curiously, this option has shown little effect under neutron irradiation. The lack of a sufficient explanation for this effect has led researchers to dub it the ”p-n puzzle,” as high-energy protons and neutrons produce similar localized agglomerations of point defects in the lattice structure of silicon, but the effects of oxygenation are much more pronounced for protons than neutrons [3].

Regardless, it is clear than annealing solves many of the issues silicon faces under heavy doses of radiation for use in high-energy physics experiments, such as those supporting research performed at CERN's LHC. However, for use as photodetectors in radiation detection experimentation, silicon's inability to relax leakage current back to pre-irradiation levels can cause significant issues when working with the relatively weak photon signals produced by scintillators, as increases in leakage current can flood out any additional current induced via the collection of scintillation photons [9].

1.2.2 Radiation Damage in Organic Photodetectors

While the applicability of silicon photodetectors for high-energy physics research has necessitated a large volume of work on the problem of radiation damage, the relative novelty of organic photodetectors [10] leaves this area largely unexplored. The area of photovoltaic research has diversified in recent years with, for example, the production of devices that incorporate organometallic materials (such as perovskite or colloidal quantum dot detectors) [10]. However, purely organic semiconductor materials show many favorable characteristics in serving as the photosensitive region in a detector, as well as being mechanically flexible and simple to fabricate [9].

The development of these organic photodiodes has proceeded largely through the lens of their eventual application in solar cells [11, 12]. The potential to use these devices di-

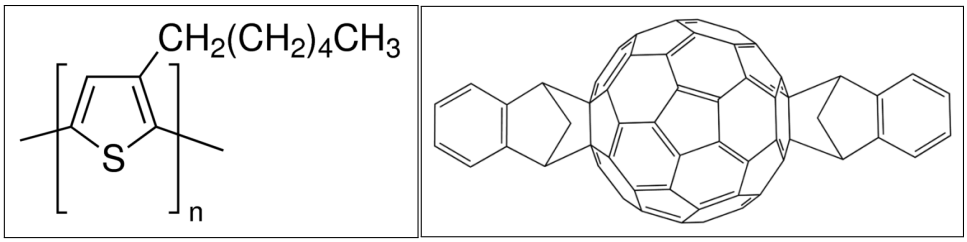

Figure 1.3: Chemical structure of P3HT (left) and ICBA (right) molecules present in the active layer of organic photodiodes used in this work.

rectly as scintillation light collectors has been largely limited by the relatively high leakage current that has been ubiquitous in OPVs to this point. However, poly[3-hexylthiophene]:indene C60-bisadduct (P3HT:ICBA) has shown exceptionally low dark current due to its relatively large bandgap energy [13]. Decreasing dark current inherently increases the overall detectivity of the organic photodiode [14]:

$$D^* \equiv \frac{R\sqrt{A\Delta f}}{I_N}, \tag{1.3}$$

where D^* is the specific detectivity of the device, R is the photodiode responsivity, A is the photodiode surface area, Δf is its bandwidth, and I_N is the noise power spectrum current. This increase in detectivity occurs in conjunction with the improvement in signal-to-noise ratio: a lower leakage current (considered to be the "noise" in this case) means that the same signal produced by incoming scintillation light will seem more prominent [9].

Though organic semiconductors (the class of devices including organic photodetectors/photodiodes) using P3HT are common in research applications, very few studies have investigated the effects of intense neutron irradiation on their performance. Being focused in particular on the use of organic semiconductors in high-energy synchrotron experiments, it is perhaps understandable that research has been focused particularly on the effects of intense x-ray beams, primarily focusing on photoelectric interactions [15, 16, 17]. Photoelectrons are produced when energetic x-rays knock out electrons in the bulk material, which are then capable of producing secondary electron-hole pairs. These electron-hole

pairs have energies between 5-20 eV, certainly enough to exceed the 4 eV necessary to break C-H and C-C bonds in the polymer chain [18]. P3HT's particular susceptibility to x-ray irradiation is primarily due to the presence of polymer side chains and the creation of atoms with high electron affinities (such as sulfur) during exposure to the beam [15]. However, the beam flux used in these experiments was on the order of 10^{15}-10^{17} $\frac{\text{n}}{\text{cm}^2\text{s}}$, on the high end of the fluxes expected from radiological sources. Given that the issues described are due in large part to photoelectron production, the effects of high doses of γ radiation must nonetheless be considered in analyzing the organic photodiodes used in this study.

Given the significant quantity of study on the issues surrounding the degradation of organic semiconductors in the presence of high x-ray and γ-ray fluences, there is comparatively little on the issue of neutron irradiation. Neutrons and γ-rays interact with materials using very different mechanisms; while γ-rays tend to interact with electrons, neutrons instead tend to undergo elastic collisions with individual atoms within the organic matrix [1]. Because hydrogen is a common component of the polymers used in these devices, this effect is known as proton recoil (though scattering on carbon and oxygen is also present, their higher masses result in less recoil and therefore, less energy imparted to the target atom). These protons deposit this energy by inducing ionization in particles along their track (though this deposition operates differently than for the secondary electrons produced by γ-ray interactions). This deposited energy induces the creation of scintillation photons in a manner similar to that of silicon.

Though this process would ostensibly result in many breaks along the polymer chain, how these breaks affect the performance of an organic photodetector has not been explored in great detail. Long-term degradation of organics has long been understood and has often been attributed to exposure to x-rays and UV light [18]. Permanent damage to some parts of the polymer chain caused during fabrication were typically not considered in studies of scintillation properties in organics, and thus this significant aspect of the long-term damage to these scintillators was ignored [19, 20]. While proton recoil is not expected to introduce

significant degradation in the operation of organic photodetectors, the high fluences used for the purposes of these experiments will be considered as a factor when leakage current measurements are taken.

CHAPTER 2

THEORY

2.1 Inorganic Semiconductor Detection Mechanism

The use of semiconductor devices for radiation detection depends on the the presence of energy bands in the crystalline lattice of materials (see schematic in figure 2.1). The valence band denotes the energy of electrons bound in shells to atoms in the lattice, and the conduction band refers to the energy level of free electrons moving through the crystal [1], though without a source of excitation, the conduction band will be empty of electrons and each valence site will be filled. The region between these two energy levels is called the bandgap, usually on the order of ca. 1 eV. The introduction of thermal excitation (e.g., through photoelectric interactions with valence sites in the crystal) can excite valence electrons to the conduction band across the bandgap, allowing these electrons to drift freely throughout the lattice. The production of this free electron necessarily creates a hole in the valence band that can also freely move through the crystal.

The effects of incident radiation (which will be considered to be a γ-ray for the purposes of this section) on a semiconductor are largely an amplification of the basic operation of a semiconductor described above. The collision of radiation with the semiconductor induces the production of an electron via either the photoelectric effect or Compton scattering. The secondary electrons produced by this incoming radiation induce ionizations along their paths, producing electron-hole pairs across the semiconductor's bandgap [21]. The electron-hole pairs created during this process induce an electric field across the bandgap, which forces electrons and holes to begin to diffuse in opposite directions through the semiconductor crystal lattice (the regions through which they migrate are known as n and p regions, corresponding to electron donor and acceptor locations, respectively). These

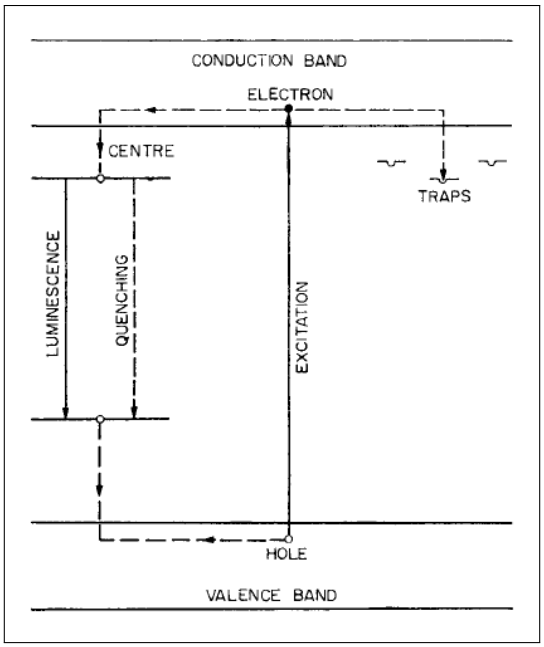

Figure 2.1: Energy band structure of an activated inorganic scintillator and potential relaxation mechanisms. Taken from [20].

charge carriers are then collected at electrodes placed at either end of the semiconductor to produce electronic pulses for the detection system. The velocity of travel through the crystal for electrons and holes is directly related to the applied electric field, and thus the migration time for each can be shortened considerably via the application of a bias voltage across the device (which, when unbiased, is on the order of 10^{-8}-10^{-9} seconds) [21].

While the creation and migration of electron-hole pairs seems very simple in the preceding description, there are several complicating factors in the application of these concepts. Of principal concern are the effects of recombination of electrons and holes prior to charge collection. Though the time required for recombination is much longer than typical electron-hole migration times (about 10^{-6} seconds), it is only in intrinsic semiconductors that such considerations apply. Physically, all semiconductors contain impurities in highly localized configurations within their crystal structure. These impurities serve as recombination centers for electrons and holes due to differences in bandgap energies for impurity atoms; lower-bandgap atoms can induce a migrating electron to combine with a migrat-

ing hole rather than traveling freely in the conduction band, forming an exciton that can decay away via photon emission rather than being collected separately at electrodes (the exploitation of these impurities is central to the operation of inorganic scintillators. [1, 21]. These impurities can also serve as electron or hole traps, which immobilize the charge carrier for a short amount of time that often results in migration times that are too long to be considered part of the measured pulse from the electrodes. As a result, the use of highly pure semiconducting material is essential to ensure that charge collection is as complete as possible.

One final consideration for semiconducting detectors is the presence of leakage current, a result of the inherent conductivity of the materials used and the inevitable presence of thermal excitations in real-world applications [1]. Statistical fluctuations in leakage current can mask the presence of radiation-induced signal currents through the semiconductor, providing a major contribution to the noise in the detector. Reducing the bias voltage across the device can mitigate some of the issues presented by leakage current, but even under small power loads (such as those to be used in this work), the issue can persist.

2.2 Organic Semiconductor Detection Mechanism

As is the case with organic and inorganic scintillators, there are several fundamental differences in the operation of inorganic and organic photodetectors. These differences are, predictably, a consequence of the configurations of molecules within organic devices. Whereas inorganic semiconductors rely on a rigid crystal structure to orient atoms and provide discrete valence and conduction electron energy bands, organic photodetectors exploit the nature of valence electron orbitals in carbon atoms to approximate these energy bands.

The structure of the polymer chains that make up organic devices necessarily requires the presence of large quantities of carbon. In its ground state, natural carbon contains four valence electron orbitals that can contain unpaired electrons; these can be shared with other atoms in order to form covalent bonds (these valence orbitals are known as the $2s$,

$2p_x$, $2p_y$, and $2p_z$ orbitals). Though these unpaired electrons lie in different orbitals, it is possible for these orbitals to mix with one another (referred to as orbital hybridization) in one of three possible configurations, allowing for the atom to form a larger range of bonds and lower the overall energy of the system [9]. Of particular interest for this application is sp^2 hybridization, in which the $2s$ and two of the three $2p$ orbitals combine to create three hybrid orbitals. The lone unhybridized $2p$ orbital (lying out-of-plane with the three hybrid orbitals) gives rise to the semiconduction capabilities of organic materials.

When two carbon atoms with sp^2 hybridized orbitals bond with one another, these bonds take one of two forms: σ-bonds or π-bonds. A σ-bond takes place between hybridized orbitals in each carbon atom, sharing two electrons between them. π-bonds, in contrast, form out-of-plane with these σ-bonds and occur between unhybridized orbitals. Because electrons in π-bonds (known as π-electrons) are further away from the carbon atoms' nuclei, these electrons tend to be more delocalized in space and result in weaker bonds than in σ-bonds.

However, these overlapping orbitals do not exist on a mere atomic level; wave function overlap between multiple carbon atoms produce what is known as a molecular orbital, which is simply a linear combination of atomic orbitals containing unpaired electrons [22]. There exist two types of molecular orbitals: those with wave functions obtained by adding the constituent atomic wave functions, known as bonding molecular orbitals, and those with wave functions obtained by subtracting their constituent atomic wave functions, known as antibonding orbitals. These molecular orbitals correspond to electron energy levels, with bonding molecular orbitals being known as π levels and antibonding orbitals as π^* levels (further dubbed the highest occupied molecular orbitals (HOMO levels) and lowest unoccupied molecular orbitals (LUMO levels), respectively). A diagram of this structure is shown in figure 2.2.

Because the polymers used for organic photodetectors are composed of very long chains of bonded carbon atoms, there is a significant likelihood that there will be large amounts

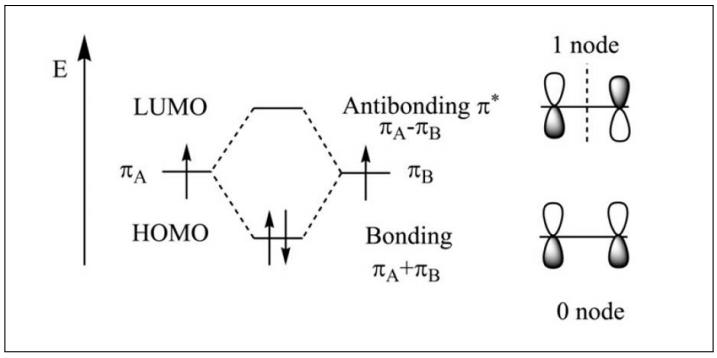

Figure 2.2: The structure of HOMO and LUMO levels in organic semiconductors via the linear combination of molecular orbitals. The right side of the figure displays the π system in the molecule. Taken from [9].

of overlap among many atomic orbitals in nearby bonded carbon atoms. This degree of overlap serves to decrease the energy gap between discrete π and π^* levels such that individual molecular orbitals essentially represent bands of energy (analogous to the valence — for π levels — and conduction — for π^* levels — bands in inorganic semiconductors) [9]. As a result, the production of electron-hole pairs is similar to that of inorganic semiconductors, though the scope of these interactions differs significantly: whereas inorganic semiconduction relies on the entire crystal structure of the bulk material, electron-hole production and migration occurs within the scope of their constituent molecular orbitals (thus making these excitation and electron-hole pair creation events largely independent of those occurring elsewhere in the polymer chain). This is could be advantageous if polymer chain breaks do indeed result during irradiation, as these breaks would not impose a significant degradation in electron-hole pair production and migration in the material as a whole.

One area in which organic photodiodes have faced significant obstacles is in the migration of charge carriers to electrodes attached to the bulk material; while excitons dissociate into free carriers readily in inorganic materials, their diffusion length in typical organic photodetectors can be as low as ca. 10 nm [23]. Thus, if exciton production is not completed near the electron donor/acceptor interface, the electron and hole will recombine without collection at their respective electrodes. The solution to this issue (utilized in the organic

photodetectors fabricated at Georgia Tech) is quite elegant in its simplicity: by merely mixing electron donor and acceptor materials, many different interfaces of the two are formed (called heterojunctions). This multitude of donor-acceptor interfaces provides electrons and holes with splitting locations well within their range, allowing them to diffuse away from one another before recombination is able to occur. These heterojunctions consist of donor-rich, acceptor-rich, and mixed phases; electrons and holes are produced and split in the mixed phase, and then are able to migrate through the acceptor- and donor-rich phases (respectively) in order to reach their respective electrodes [24].

CHAPTER 3
METHODS

Experimental work for this project consisted primarily of leakage current measurements taken both with and without radiation sources present. In addition to this experimental work, simulation models were developed in the MCNP6 to provide estimations for the amount of radiation damage induced during irradiation; the structure and specifications of said models are described in detail below.

3.1 Photodetector Irradiation and Leakage Current Measurements

3.1.1 Experimental Setup

Irradiation of organic and silicon photodetectors was performed in the Boggs Building of the Georgia Institute of Technology at the Radiological Science and Engineering Laboratory (RSEL). Due to the high neutron/γ-ray fluences present during irradiation, the well-shielded neutron generator vault of the RSEL was used for these experiments (though the less well-shielded high bay was also used for early experiments, the large amount of additional shielding required made this option less desirable). A high-activity americium-beryllium (AmBe) neutron/γ-ray source was used to irradiate the materials; though other sources were considered for the experiment, the high activity of the source was preferred to reach the fluence values desired without occupying laboratory space for a prolonged period.

The AmBe source was placed into a concrete collimator box within the neutron generator vault; while the use of this collimator box would suggest the use of a collimated neutron/γ-ray beam incident on the devices, this was not of primary concern for this experiment. As maximizing the incident flux on the devices was of primary importance, the small volume of the concrete box provided a convenient geometric size for source neutrons

Figure 3.1: Concrete collimator box containing photodetector devices and graphite holder for AmBe. Devices can be seen taped to outside of source holder. AmBe source not shown.

and γ-rays to interact with the devices via both primary interactions and after scattering. Placing the source in a concrete medium also reduced the neutron flux outside the box to a more manageable level, ensuring that the experimenters could perform measurements while safely below absorbed dose thresholds for both radiation workers and the public (both of whom were present for experimentation). Also present inside the concrete collimator box were the organic and silicon photodetectors to be observed. These devices were taped to the outside of the AmBe's graphite holder at a distance of 2 cm from the edge of the spherical AmBe source (a photograph depicting the location of the devices relative to the source is included in figure 3.1). These devices were covered with electrical tape in order to ensure complete isolation from ambient light (a necessity in the measurement of leakage current). This light isolation also required turning off all light sources inside the neutron generator vault during experimentation.

Real-time measurement of leakage current fluctuations under irradiation required a

monitoring system accessible to humans without exposure to the high fluxes present in the laboratory, and thus extensive preparation was required before an experiment could begin. Organic photodetectors required connection to a Keithley 6517 electrometer via a 30 foot BNC coaxial cable to provide it bias voltage. In addition, 30 foot BNC cables were required to ground the device, and additional (shorter) BNC cables were used to connect the electrometer to a DC power supply. Cables connected to the device inside the laboratory were run through pipes connecting the neutron generator vault to a control room located just outside the well-shielded generator vault door. These were then connected to the electrometers and power supply. Output from the electrometers was passed to a computer running a purpose-built LabView 2012 program to measure and plot the leakage current of the device. A schematic of this experimental setup is shown in figures 3.2a and 3.2b.

3.1.2 Experimental Procedure

Setup of devices and relevant measurement and analysis equipment was performed prior to the introduction of the AmBe source to the experiment in order to minimize human exposure (gloves and external dosimetry were required throughout this experiment). A short (ca. 5 minute) baseline measurement of leakage current was taken for the device prior to irradiation. This was followed by the introduction of the AmBe source. The source was placed in its graphite holder and the collimator box was shut. Radiation meter surveys were performed at a distance of 3 feet from the collimator box in every direction in order to discern the maximum dose rate from the source in the immediate vicinity of the source. Dose measurements were highest on the side of the box containing the collimator; accordingly, the collimator was faced away from the vault's door. Additional survey measurements were performed at the entrance to the neutron vault prior to exiting. After these surveys were complete, the lights in the generator vault were turned off and the door to the generator vault was closed. Additional radiation meter surveys were performed to ensure that the combined neutron and γ-ray dose levels at the door to the vault were below the threshold

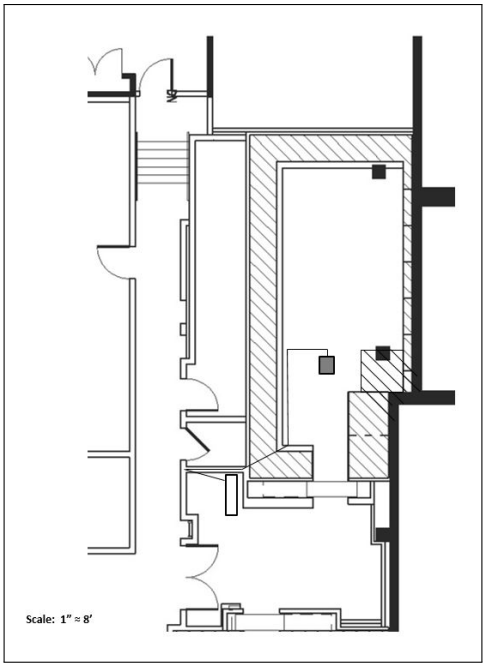

(a) Floor plan of the laboratory used for photodetector irradiation experiments. Note the presence of the concrete collimator box in the neutron generator vault. Cables were fed from the southwest corner of the neutron generator vault to the northwest corner of the control room.

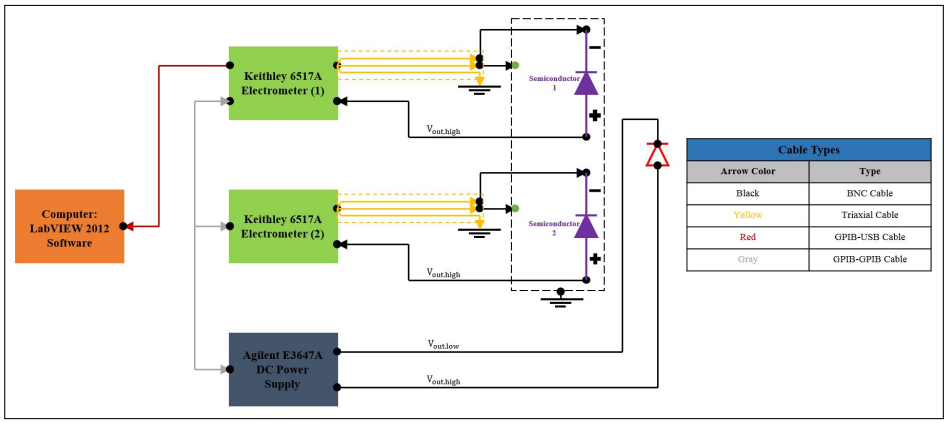

(b) Schematic of irradiation experimental setup. Green circles represent guards against large voltage fluctuations through photodetectors; red diode represents an LED signaling connectivity between electrometers and the photodetector. Objects placed in collimator box with source are enclosed in dashed box. Current signals are passed through both electrometers to the LabVIEW program on the computer for analysis.

Figure 3.2: Overall irradiation experimental setup.

of 2 $\frac{\text{mrem}}{\text{hr}}$. The dose rate map for the experimental area was then posted on the door to the vault along with signage indicating an area of high radiation.

At this point, measurements could begin: leakage current was measured in real-time for irradiation times of 20 hours per sample. At $\phi_{neutron} \approx 8.57\text{x}10^{12} \frac{\text{n}}{\text{cm}^2}$ and $\phi_{\gamma} \approx 4.91\text{x}10^{12} \frac{\gamma}{\text{cm}^2}$, these values lie comfortably in the ranges typically reported in literature results [25, 26]. The experimental setup, being located in a secure area, was able to be left alone for the bulk of the 20 hour run time. When irradiation was completed, leakage current measurements ceased, and the door to the generator vault could be opened. The AmBe source was relocated to its storage container and the experimental setup could be dismantled. The device was removed from the collimator box and stored for later performance measurement and analysis.

In addition to these leakage current measurements performed during photodetector irradiation, further measurements were taken after the device had been away from the presence of radiation for a significant amount of time. Without the presence of radiation, these experiments could be performed in a relatively simple laboratory setting; while the experiment design followed that shown in 3.2b, the setup did not require the extensive safety measures taken during irradiation, and thus could take place outside of the neutron generator vault of the RSEL (experiments were performed in the Center for Organic Photonics and Electronics in the Molecular Sciences and Engineering building at Georgia Tech). The device was covered in black electrical tape for ambient light isolation, though enclosure in a light isolation box (such as the collimator box used in irradiation experiments) was not necessary. The leakage current of the device was again measured for the same 20 hour run time as in irradiation experiments.

3.2 MCNP Simulations

Though not traditionally a simulation package centered around modeling radiation damage, MCNP's ubiquity throughout the nuclear community makes it an attractive option for this

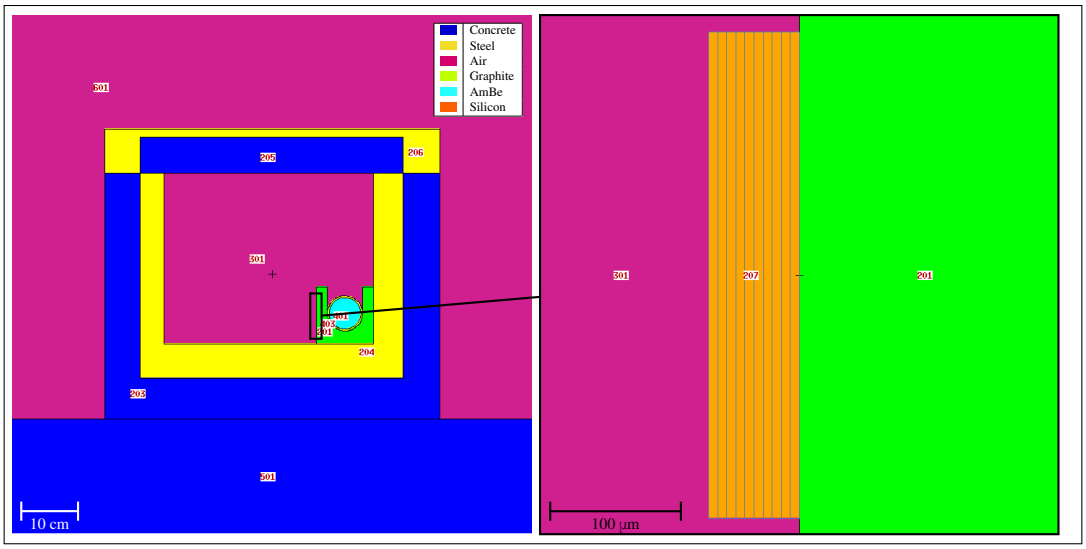

Figure 3.3: Typical MCNP problem geometry using silicon photodiode. Numbers indicate problem cells. Magnified region displays SiPD (cell 207). Gray lines in magnified region denote meshes used in mesh tallies.

application. However, MCNP was chosen as the preferred method for modeling irradiation experiments due not only to its convenience, but also its versatility; given a known energy-dependent fluence and reasonable problem geometry, MCNP can be employed to calculate any neutral particle reaction rate that possesses an associated Evaluated Nuclear Data File (ENDF) cross-section library [27]. To this end, MCNP6 was utilized to develop models capable of determining the dose rate delivered and the total atomic displacements per atom (DPA) per unit time in both silicon and organic photodiodes (example MCNP input files are included in Appendix A).

3.2.1 Description of Model Geometry

Problem definition in MCNP6 is governed by the use of an input file consisting of sections (called ”cards” within MCNP) that define the geometric and physics specifications of the problem. Geometric definition for these irradiation experiments was fairly detailed, incorporating the collimator box used as the primary experimentation space, as well as the AmBe source and its graphite holder (see figure 3.3).

The geometry is defined by the collimator box (cells 203-206), the graphite AmBe

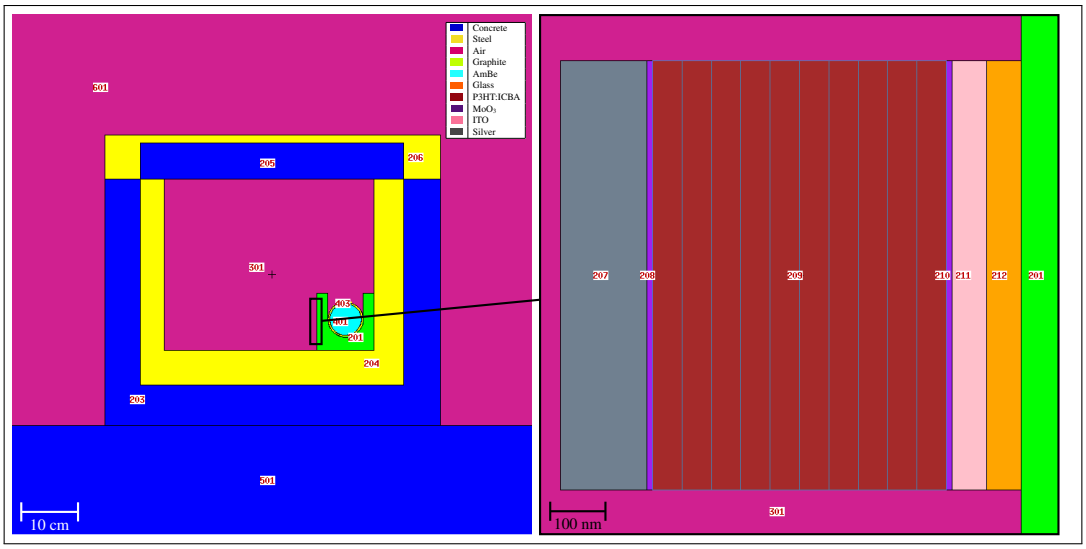

Figure 3.4: Typical MCNP problem geometry using organic photodiode. Numbers indicate problem cells. Magnified region displays OPD (cells 207-212). Gray lines in magnified region denote meshes used in mesh tallies.

holder (cell 201), the AmBe source (cells 401 and 403), the floor of the laboratory space (cell 501), and the air inside the collimator box and surrounding the total geometry (cells 301 and 601, respectively). An additional setup was also tested, incorporating the entirety of the lab space; however, the extremely minuscule size of the photodiodes used and the lack of secondary contributions from the walls of the lab space to the dose/flux in the photodiode made this level of detail unnecessary (the floor was included due to the significant neutron albedo contribution to the flux through the photodiode, however). While the structure of the geometry remained largely similar between photodiode compositions, the layered nature of the organic photodiodes allowed for finer splitting of the geometry. This resulted in a very accurate representation of the design of the organic photodiodes, but introduced significantly more physical uncertainty as a necessary consequence.

3.2.2 Description of Model Physics

Determining the dose and flux delivered to each photodiode required delicate physics specifications, largely as a result of the relative size of the devices when considering the scope of the problem. The AmBe source neutron spectrum information was incorporated using

Standard 8529 for a bare AmBe source from the International Organization of Standards [28], which has since been modified using updated methodologies [29]. The γ spectrum of bare AmBe, in contrast to its neutron spectrum, consists of only a few discrete energies. While ^{241}Am radioactive decay produces several low-energy γ-rays, its 59.5 keV emission is the most intense and thus the most likely to contribute to the γ flux reaching the photodetectors. However, simulations of the γ flux reaching these photodetectors with this emission included indicated that only about 0.01% of these γ-rays were transported through the AmBe's steel shell and the graphite source holder to reach these photodetectors. As a result, this emission was excluded from the set of final simulations for this project.

By far the most prominent γ-ray emission from AmBe comes from the interaction of the 5.49 MeV α particle produced via ^{241}Am radioactive decay with ^{9}Be inside the source itself:

$$^{9}\text{Be} + \alpha \rightarrow {}^{12}\text{C}^{*} + \text{n}$$

This is the primary neutron-producing interaction within an AmBe source, but also serves to produce its most intense γ-ray emission. The excited ^{12}C nucleus produced in this reaction decays via 4.438 MeV γ-ray emission, and it is this γ-ray that serves as the primary source of the AmBe γ-rays. Therefore, for the purposes of this AmBe model, a monoenergetic 4.44 MeV γ-ray was added to the source term. γ-rays were produced along with neutrons at a ratio of 0.573:1 based on experimental data obtained from literature [30].

Determination of material composition was performed largely based on published MCNP standards [31], though compositions of the organic photodiodes used were determined using relative atomic weights in the compositions of the constituent polymers. Determination of flux and dose contributions in photodiode cells were calculated using cell-averaged flux (`F4`) and energy deposition (`F6`) tallies. These tallies were each multiplied by various factors as well to obtain the desired quantities and units: flux tallies were adjusted to obtain units of displacements per atom (DPA), while energy deposition values were converted to rads ($\frac{\text{ergs}}{\text{g}}$) from MCNP's conventional $\frac{\text{MeV}}{\text{g}}$ (this conversion is performed by using a tally

multiplier (FM) card for F6 tallies). While dose calculations required only minor corrections to obtain conventional units, however, conversion of output flux values to DPA information required many more complex changes.

3.2.2.1 Modifications of ENDF/B-VIII Cross-Section Libraries using NJOY

In order to convert flux values to DPA, modification of ENDF/B-VII neutron and photoatomic cross-section libraries (hereafter referred to as ENDF libraries) as well as MCNP's F4 tally were required; calculation of DPA uses the total damage cross-section for a material, a quantity that relies on the amount of damage energy an incident particle can impart on that material and the amount of energy required in order to displace an atom from its position in the material's lattice [32]. For neutrons, these quantities can be combined with the total cross-section for the material to yield the total DPA cross-section for the material via the relation [33]:

$$dpa = \frac{\int dV \int \phi(\vec{r}, E) dE \sum_{i=1}^{N} X_i \frac{1}{E_{d,i}} \sigma_i^{dpa}(E)}{2 \sum_{i=1}^{N} E_{d,i}}, \tag{3.1}$$

where $\phi(\vec{r}, E)$ is the neutron flux at position $\vec{r}$ and energy E, V is the volume of the cell in question, X_i is the atomic density ($\frac{\text{atoms}}{\text{barn-cm}}$), $E_{d,i}$ is the energy required to displace one atom of type i, and $\sigma_i^{dpa}(E)$ is the DPA cross-section of said atom at neutron energy E. The threshold energy required for atomic displacement, E_d, is dependent on the material in question and has been determined experimentally. The values used for E_d in this experiment are included in Table 3.1.

Table 3.1: Atomic displacement threshold energies for materials used in photodetectors for this experiment. Hydrogen omitted due to lack of room-temperature data.

Element	Displacement Threshold Energy (eV)	Source
Silicon	25	[34]
Carbon	33	[35]
Sulfur	9.6	[36]

For photoatomic interactions, partial kerma heating factors (effectively serving as photon damage cross-sections) must be computed for individual interaction types (described below) over multiple photon energy groups. Using known photoatomic interaction cross-sections, an understanding of the photon flux involved in the problem in question, and an optimized group structure, cross-sections can be converted to heating factors via the relations:

$$\sigma_{xg} = \frac{\int_g \sigma_x \phi_0(E) dE}{\int_g \phi_0(E) dE}, \tag{3.2a}$$

$$\sigma_{T\ell g} = \frac{\int_g \sigma_T(E) \phi_\ell(E) dE}{\int_g \phi_\ell(E) dE}, \text{ and} \tag{3.2b}$$

$$\sigma_{x\ell g \to g'} = \frac{\int_g \mathscr{F}_{x\ell g'}(E) \sigma_x(E) \phi_\ell(E) dE}{\int_g \phi_\ell(E) dE} \tag{3.2c}$$

where g is the energy group for initial photon energy E, g' is a group of final photon energies E', x is one of the photoatomic reaction types (described below in the definition for GAMINR), T denotes a total value, ϕ_ℓ is a Legendre component of a guess for the photon flux encountered, σ_g is a total kerma factor for photons of energy group g for all photoatomic interactions, and $\mathscr{F}$ is a feed function describing the total normalized probability of a photon scattering from initial energy E into group g' of interaction type x [37].

Because MCNP performs volume and energy integration implicitly and outputs flux as the `F4` tally, only the summation terms in equation 3.1 must be determined by the user. However, because the DPA cross-section is dependent on material-specific energies as well as the incident neutron energy and must be summed over all materials in the relevant region (i.e., all present silicon isotopes in silicon photodiodes or hydrogen, carbon, and sulfur in organic photodiodes), these cross-sections must be evaluated in addition to the traditional ENDF libraries. This issue is compounded in the case of photoatomic interactions, which require prior knowledge of the photon fluxes involved while also being reliant on the energy of the photons under consideration.

In order to implement these cross-sections, the NJOY code [38] was used to convert ENDF data into an application-suitable format using input files. The format of NJOY input is similar to MCNP (both being written in Fortran), consisting of a series of ”cards” that are read in sequence to process ENDF data. NJOY is split into several modules, each adjusting or processing ENDF data to fit a specific application. In order to derive DPA cross-sections, the RECONR, BROADR, MODER, HEATR, GAMINR, and ACER modules were utilized [37]:

- **RECONR**: Converts traditional ENDF files into pointwise cross-section information using resonance parameters and interpolation methods,
- **BROADR**: Applies Doppler broadening to cross-sections at user-specified temperatures,
- **MODER**: Converts ENDF files between ASCII and binary modes,
- **HEATR**: Generates radiation damage production cross-sections and kerma factors (or heat production cross-sections),
- **GAMINR**: Generates multigroup photoatomic cross-section libraries from ENDF data, incorporating coherent, incoherent, pair production, photoelectric, and total cross-sections (denoted as x in photoatomic equations),
- **ACER**: Converts raw ENDF data to ACE table format suitable for implementation alongside other cross-section data in MCNP.

The NJOY procedure for an individual library was as follows (note: each filename used in the NJOY process, both input and output, follows the nomenclature ”tapeXX”, where XX is the number used to identify that particular file in the NJOY input file; positive numbers refer to ASCII data, while negative numbers refer to binary data):

- 1. Using MODER, the standard ASCII ENDF library was converted to binary – this allows for quicker cross-section computation time, as the time required to convert the data was less than processing ASCII data through individual modules.

- 2. RECONR was run to produce a pointwise ENDF (PENDF) file for simple interpolation during calculation.

- 3. The PENDF library was Doppler-broadened using BROADR at a specified temperature (taken to be 293.6 K, the temperature of the lab environment for these experiments).

- 4. HEATR was applied, generating radiation damage energy cross-sections from the PENDF library using:

$$D(E) = \sigma(E) \int_{-1}^{1} f(E, \mu) P(E_R[E, \mu]) d\mu \tag{3.3}$$

where $f(E, \mu)$ is the angular distribution in `MF=4` of the ENDF library for the material in question [37], and $D(E)$ is the damage energy production cross-section. The total damage energy production cross-section was requested using `MT=444`.

- 5. Damage cross-sections for photoatomic interactions are produced using GAMINR, summing the partial kerma factors for each interaction to obtain multigroup heating factors using:

$$\sigma_{Hxg} = \frac{\int_g [E - \bar{E}_x(E)] \sigma_x(E) \phi_0(E) dE}{\int_g \phi_0(E) dE} \tag{3.4}$$

where $\bar{E}_x(E)$ is the average energy of photons with energy E scattered by reaction type x and ϕ_0 is the Legendre component of an initial guess for the photon flux [37]. The heating factor for these photon interactions was accessed using `MT=525`; rather than in the case of neutron heating, where a tally multiplier was needed in order to

specify the reaction that contributes to radiation damage, photoatomic heating reactions are assumed to be displacement reactions and did not require a tally multiplier; therefore, only the modification of cross-section data was necessary to incorporate radiation damage effects by γ-rays.

- 6. Damage cross-section data is output to an ACE-style format using ACER, which produces the ACE-mode data and a separate line of information to add to the XSDIR file that MCNP uses to refer to the location of ACE data in memory. A unique ZAID suffix used in specifying a cross-section library's particular information (e.g., .80c for ENDF/B-VIII continuous data) was also specified in order to avoid conflicts with existing ENDF library data.

- 7. The ACE file was added to the correct file system sub-folder under `$DATAPATH/xdata` in order to be retrieved by MCNP during simulation.

Example NJOY input following this procedure is provided in Appendix B utilizing these modules. The neutron DPA cross-section data produced by NJOY was then accessed via the tally multiplier card in MCNP by specifying reaction number `MT=444` be used for the `F4` tally (in addition, if a separate `xsdir` file was created to avoid conflicting with MCNP's default, that file must be specified on the command line when executing the relevant job via the `xsdir` option). The incident neutron energy independence of all quantities in equation 3.1, aside from the DPA cross-section and the neutron flux, allows these quantities to be collapsed into a single tally multiplier factor, taking the form:

$$\frac{\sum_{i=1}^{N} X_i \frac{1}{E_{d,i}}}{\sum_{i=1}^{N} X_i} \tag{3.5}$$

This form of the tally multiplier factor, combined with the material number in question and the reaction number, are the only quantities to be specified in order to convert the `F4` tally into a DPA tally (using, of course, NJOY-modified neutron cross-section data). In

the case of silicon photodiodes, the conversion value was 1002.9; with the more complex organic photodiodes, the value was 13.9.

While standard F tallies were useful in obtaining bulk measurements of dose and DPA in photodiodes, of particular interest was determining the geometric distribution of these quantities throughout the photodiodes in question. Because the photodiodes used are very thin in relation to the problem geometry on the whole, it was important to learn whether thicker samples would provide a significant change in the number of particles displaced due to neutron irradiation or the amount of time needed to satisfactorily irradiate the samples. In order to do this, mesh tallies could be superimposed over the problem geometry, which allows the user to avoid splitting the photodiodes into individual cells manually. The FMESH card allows the user to impose an F4 tally over a user-defined mesh (in this case, the photodiodes were meshed depth-wise only, as shown in figures 3.3 and 3.4). Because FMESH only allows the use of volume flux tallies, however, the TMESH card was utilized to obtain dose deposition data. While TMESH offers more tallying versatility (rivaling that of standard F tallies), it suffers from two main drawbacks: analysis of output data relies on the cumbersome GRIDCONV auxiliary program, and, as TMESH is a legacy feature from the charged particle-based MCNPX, problems using it cannot be parallelized (adding significantly to the run time for each simulation). In contrast, FMESH data is output to a simple text file and supports parallelization. Fortunately, tally multipliers can be used with both mesh tallying methods, allowing for direct comparison between results obtained using both meshing techniques.

CHAPTER 4
RESULTS AND DISCUSSION

4.1 Simulation Results

4.1.1 Damage Cross-Section Calculations

As a necessary prerequisite to the development of an MCNP model for this project, the ENDF/B-VIII cross-section libraries (referred to hereafter as "ENDF libraries") for the silicon and organic photodiode materials required modification through the use of NJOY. Using the six modules outlined in section 3.2.2, the data in the ENDF libraries for silicon, as well as hydrogen, carbon, and sulfur (the constituents of P3HT:ICBA) were processed, adding radiation damage energy production cross-sections and photon heating factors to these libraries for each material. As they are dependent primarily on photoatomic interactions, photon heating values could be compared on an equal basis between materials. However, due to a bug in the publicly-available version of NJOY (known as NJOY2016; this bug does not exist in LANL-controlled NJOY99), GAMINR-modified photoatomic heating data could not be converted into the ACE format suitable for plotting; as the raw photoatomic data contains many of the same trends found among the heating factor data, though, it is included in figure 4.1 (the sulfur component has been omitted from this figure and the neutron cross-section figures to follow due to P3HT:ICBA consisting of $<1\%$ sulfur by atom and $<3\%$ by weight). With a few exceptions in the keV range, the silicon photoatomic cross-section is consistently greater than that of the components of P3HT:ICBA, and this greater interaction rate will likely induce a greater volume of atomic displacements in silicon as a result.

As with the photoatomic data, neutron cross sections required further manipulation to achieve suitable radiation damage cross-section data. While the implementation of

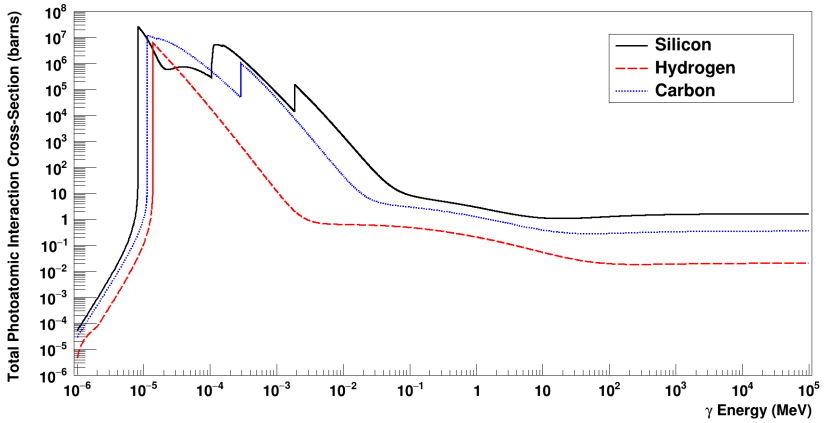

Figure 4.1: Comparison of total photoatomic cross-sections of silicon and the carbon and hydrogen components of P3HT:ICBA.

the P3HT:ICBA mixture microscopic neutron cross-sections is handled on a particle-by-particle basis within MCNP (therefore requiring no further manipulation for simulation purposes beyond NJOY processing), in order to provide a visual representation of how these neutron cross-sections vary in comparison to silicon, microscopic cross-sections were converted to macroscopic via the familiar relation

$$\Sigma_{total} = \sum_{i=1}^{n} N_i \sigma_i \tag{4.1}$$

where Σ_{total} is the total macroscopic neutron damage cross-section for the mixture ($\frac{\text{MeV}}{\text{cm}}$), σ_i is microscopic neutron damage cross-section for constituent material i (MeV-barns), and N_i is the atomic density of constituent material i ($\frac{\text{atoms}}{\text{cm}^3}$), defined as

$$N_i = \frac{\rho_i N_A}{A_i} \tag{4.2}$$

where ρ_i is the mass density of the constituent ($\frac{\text{g}}{\text{cc}}$), N_A is Avogadro's number (6.02x10^{23} $\frac{\text{atoms}}{\text{mol}}$), and A_i is the molar mass of the constituent ($\frac{\text{g}}{\text{mol}}$). As is shown in figure 4.2b, silicon maintains a higher damage cross-section (primarily due to its comparatively higher atomic density) up to energies around 1 MeV, after which the organic mixture undergoes a marked

increase in cross-section, a phenomenon largely attributable to a corresponding set of resonances in carbon's microscopic cross-section at those energies, as indicated in figure 4.2a. This fundamental probability information suggests that, over a wide range of neutron irradiation energies, silicon should be prone to greater damage effects than the organic mixture used in this project's photodiodes. However, this hypothesis also relies on knowledge of the energy spectrum of neutrons interacting with each device, which is a slightly softer form of the traditional AmBe spectrum.

4.1.2 Source-Detector Efficiency Considerations

4.1.2.1 AmBe Neutron Energy Spectrum Moderation

While the neutron spectrum of a bare AmBe source has been standardized (see section 3.2.2), the energy spectrum of neutrons reaching the photodetectors themselves is reshaped by neutron interactions in the steel shell surrounding the AmBe, the graphite block holding the AmBe in position (and to which the photodetectors were attached), and the concrete and steel interior walls of the collimator box. In order to determine how this energy spectrum had changed in passing through these materials, an additional measurement was added to the MCNP model developed for this project to detect the flux of neutrons through the interface between the graphite block and the photodetector exterior. These flux values were then binned in energy using the same structure as in the AmBe source definition and compared to the raw source spectrum (the results of which are shown in figure 4.3a). Though a significant fraction of neutrons interact in the photodetectors with energies >1 MeV, the energy spectrum has been strongly moderated, and the majority of neutron interactions occur at energies at which the radiation damage cross-section in P3HT:ICBA is significantly lower than in silicon (as indicated in figures 4.2a and 4.2b). This serves to further support the hypothesis that these organic photodetectors will undergo less radiation damage due to neutrons than their silicon counterparts, assuming similar geometry between the devices.

A similar, yet muted, level of moderation of the AmBe's γ-ray spectrum also occurred

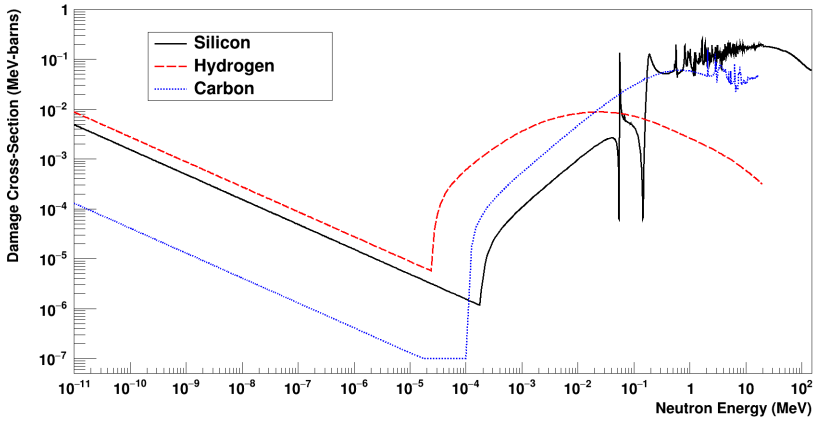

(a) Comparison of microscopic radiation damage cross-sections of silicon and the carbon and hydrogen components of P3HT:ICBA.

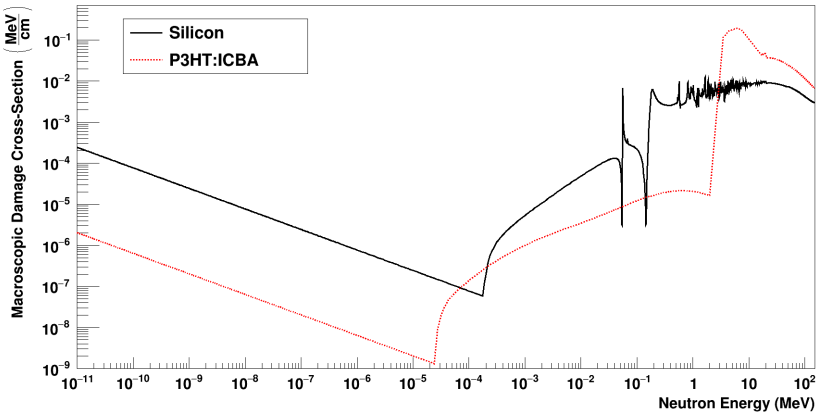

(b) Macroscopic radiation damage cross-sections for silicon and the organic P3HT:ICBA under neutron irradiation.

Figure 4.2: Neutron damage cross-section plots for organic and silicon photodetector components.

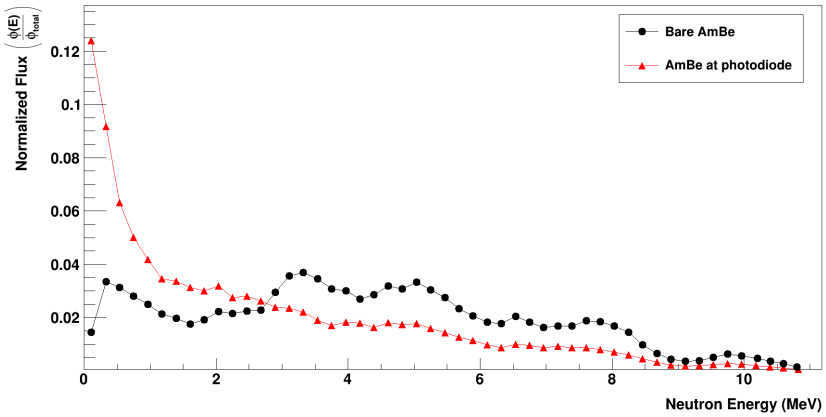

(a) Comparison of the bare AmBe neutron energy spectrum to the steel- and graphite-moderated spectrum seen at photodetector exterior (error bars in moderated spectrum are smaller than symbol size).

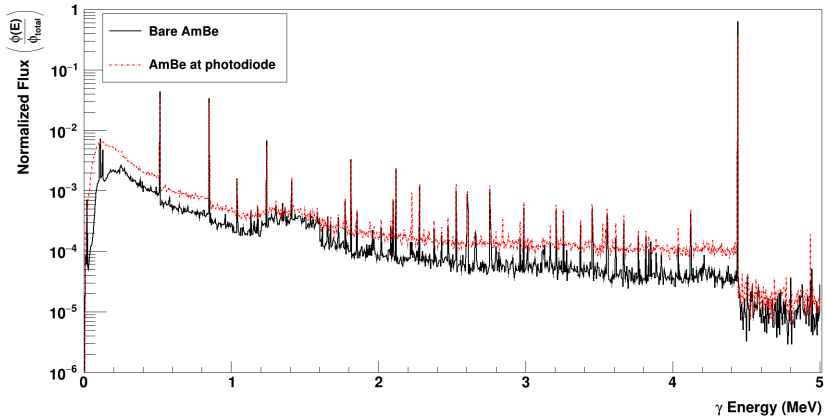

(b) Comparison of the bare AmBe γ-ray energy spectrum to the steel- and graphite-moderated spectrum seen at photodetector exterior (error bars in moderated spectrum are smaller than symbol size).

Figure 4.3: Moderated and unmoderated energy spectra for neutrons and γ-rays produced by an AmBe source.

as a result of interactions with experiment materials. As discussed in section 3.2.2, the 4.438 MeV γ-ray emission was the only source γ created; however, the production of γ-rays due to interactions within the source and with experiment materials introduced several less intense γ-rays as well. Using the same technique as with the moderation of the neutron spectrum, the effect of these interactions was quantified using MCNP, but with energy bins that were equal in width between 0-5 MeV. The flux of γ-rays was measured at the outer edge of the AmBe material in the source and compared to the flux at the photodetector exterior (the results of which are shown in figure 4.3b). Though the energy spectrum at the photodetector has been noticeably moderated by experiment materials, the effect of these materials is less impactful than in the moderated neutron spectrum. This is largely due to the fact that the steel and graphite moderating these γ-rays are low-Z materials, which are far more transparent to γ radiation than to neutrons. Similar to the neutron case, the γ-ray energy spectrum seen by these photodetectors also corresponds to an energy range at which the photoatomic interaction cross-section for silicon is higher than in the components of P3HT:ICBA (shown in figure 4.1), which also supports the suggestion that silicon devices will experience a higher rate of radiation damage than their organic counterparts.

4.1.2.2 Calculation of Source-Detector Geometry Factor

The effect of source-detector geometry (the "detector" in this case referring specifically to the photodetector in question) within the experimental design has a significant impact on the the total number of particles seen by the detector; as the AmBe source is an isotropic, volumetric source of particles, the large majority of its emitted neutrons and γ-rays will not travel in the direction of the detector (an effect further exacerbated by the presence of the AmBe's steel shell and its graphite holder). Because MCNP's tally information is always provided on a per-source particle basis, calculating the number of particles actually traveling through the region of interest is essential in normalizing tally results correctly. The ratio of particles emitted from a source of known geometry and those particles traveling in

the direction of a detector of known geometry is referred to as the source-detector "solid angle" or geometry factor. But while solid angle calculations involving point and cylindrical sources and detectors are fairly trivial, the use of a spherical source in this experiment provided a slightly more challenging case. Therefore, three approaches, two analytical and one stochastic, were utilized in order to quantify the solid angle for this design.

The first of these techniques involved approximating the source and detector as disks of arbitrary thickness (shown in figure 4.4a) and applying a known analytical formula to solve for the solid angle. While this provided a much more straightforward framework than would be needed in deriving a solid angle formula for this particular geometry, both source and detector geometries are approximated (the spherical source and rectangular detectors as cylinders) and it is likely that the solid angle will be overestimated as a result. The calculation for this geometry factor is governed by averaging the solid angle over the surface of the source via the integral [39]

$$\Omega = \frac{4\pi a}{s}\int_0^\infty \frac{e^{-dk}J_1(sk)J_1(ak)}{k}dk \tag{4.3}$$

where Ω is the solid angle subtended by the detector at the source position (steradians), J_1 is a Bessel function of the first kind, and the dimensions s, a, and d are lengths specified in figure 4.4a. Solving via numerical integration yields the following set of equations:

$$\Omega \approx \frac{1}{2}[1 - \frac{1}{(1+\beta)^{\frac{1}{2}}} - \frac{3}{8}\frac{\alpha\beta}{(1+\beta)^{\frac{5}{2}}} + \alpha^2[F1] - \alpha^3[F2], \tag{4.4a}$$

$$F1 = \frac{5}{16}\frac{\beta}{(1+\beta)^{\frac{7}{2}}} - \frac{35}{16}\frac{\beta^2}{(1+\beta)^{\frac{9}{2}}}, \text{and} \tag{4.4b}$$

$$F2 = \frac{35}{128}\frac{\beta}{(1+\beta)^{\frac{9}{2}}} - \frac{315}{256}\frac{\beta^2}{(1+\beta)^{\frac{11}{2}}} + \frac{1155}{1024}\frac{\beta^3}{(1+\beta)^{\frac{13}{2}}} \tag{4.4c}$$

where $\alpha = (\frac{s}{d})^2$ and $\beta = (\frac{a}{d})^2$. Applying this approximation to the source-detector design in this experiment yielded a solid angle value $\Omega = 0.117$ sr, suggesting that 11.7% of particles emitted from the source would reach the detector.

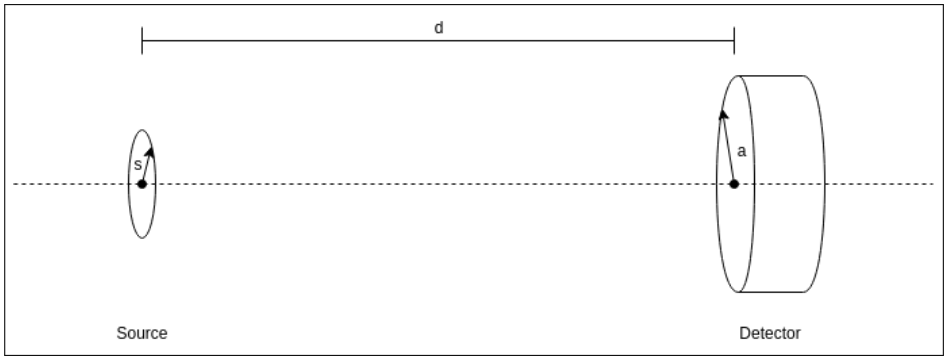

(a) A diagram of the disk approximation for source and detector.

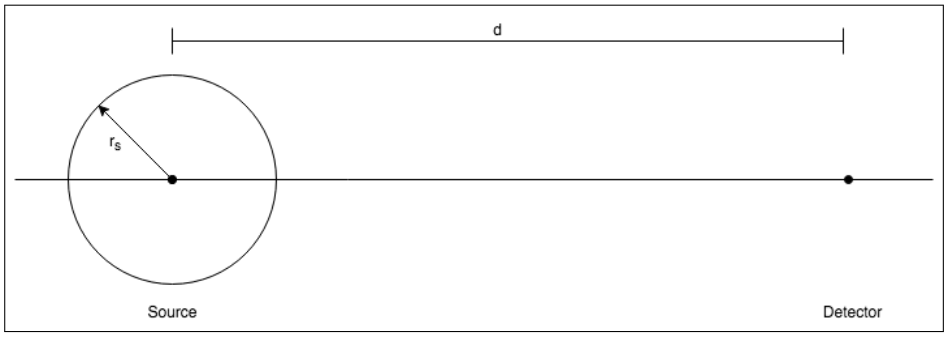

(b) A diagram of an experimental geometry using a spherical source and a point detector.

Figure 4.4: Analytic solid-angle approximations used for this experiment.

The second technique used to analytically calculate the geometry factor for this setup involved approximating the photodetectors as point detectors, but making no simplifications to the source geometry (i.e., a spherical source-point detector solution). This design is shown in figure 4.4b. Though no geometric approximations were required in this calculation, for simplicity, the spherical source is assumed to emit particles from its surface, rather than throughout its volume. While source self-scattering and scattering due to the steel shell around the physical source would certainly introduce some anisotropy, these effects were assumed to be small in the pursuit of an analytic solution. With this simplification, the solid angle can be determined using a single simple equation [40]:

$$\Omega = \frac{1}{4\pi d^2} \tag{4.5}$$

Using this formulation yields a solid angle value of only $\Omega = 0.064$ sr, or 6.4% of source particles, or nearly two times lower than with the disk approximation of the geometry factor for this experiment. This disagreement between solid angle results suggested that a viable analytic solution using geometric approximations was unlikely to be found.

The use of a stochastic solution in the determination of solid angle provided a method to reduce the amount of simplification required when using analytic approaches. Rather than attempting to develop an adequate formula to summarize the geometry of the problem, the MCNP model developed for the purposes of this experiment could be used to check the validity of these divergent analytic solutions. To do this, the current of neutrons and γ-rays across the surface of the photodetector facing the source was measured using an `F1` tally (and tallying only particles traveling through the photodetector from the direction of the source by specifying the directionality of tallied particles). Because the source and detector could be modeled exactly as in the physical experiment, this method would include no geometric approximations, while also incorporating the graphite AmBe holder that further affected the isotropy of the physical source. Using this technique, a solid angle value of $\Omega = 5.97\text{x}10^{-5}$ sr was obtained, suggesting that the analytic solutions used were

overpredicting the geometry factor in this problem by several orders of magnitude. This disagreement between stochastic and analytic methods is likely due to a combination of the geometric approximations made to fit this problem's geometry to known formulas and the high likelihood of scatter within the graphite block. Because the analytic approaches were not able to quantify the effects of scatter (only considering uncollided particles), for the purposes of normalizing MCNP measurement results, the stochastic value of $\Omega = 5.97\text{x}10^{-5}$ was used in calculations.

4.1.3 MCNP Simulation Results

As is described in section 3.2.2, simulation of radiation damage in photodetectors was determined using three different MCNP tallying techniques (using the same tally multipliers for each): via track-length estimation of particle flux averaged over the volume of the entire cell (the `F4` tally), as well as two mesh tallies also estimating particle flux via track-length, but averaged over the volume of individual meshes (the aforementioned `FMESH` tally and `TMESH` Type 1 tally). (Note: because the photoactive region of photodetectors tend to be very thin (ca. 510 nm for organic devices and ca. 0.7 mm for silicon), mesh tally data did not vary significantly between mesh regions and largely served to confirm the results obtained with standard tallies; these results will not be reported unless diverging significantly from standard tally results). As the energy deposited in photodetectors was suspected to correlate significantly with the amount of radiation damage undergone, `F6` (energy deposited per unit mass of a cell) tallies as well as additional `TMESH` Type 1 tallies were recorded to investigate this correlation. Each of these measurements were performed for both neutrons and photons and recorded simultaneously.

While the organic devices used in this work were of much smaller thickness than with silicon, the other dimensions of the photodetectors were assumed to be similar for the purposes of simulation even though the OPDs used in physical measurements were of slightly larger dimensions. This is because the dimensions provided for OPD samples were mea-

sured at the greatest extent of the glass layers enclosing the photoactive region of the device instead of just the P3HT:ICBA layer; though the photoactive area itself is not visible in the final product, the rough similarity in size between the SiPDs used and the layers enclosing the OPD photoactive layer suggested that this assumption was reasonable. In addition, assuming consistency in photodetector dimensions allowed for the same solid angle (or geometry factor) value to be assumed for each device (see section 4.1.2.2), simplifying the hand calculations required to renormalize tally results by the number of source particles.

While the basic objective of these simulations is to provide a theoretical basis for the current and voltage response data collected during physical experimentation, additional simulations were performed in order to quantify the effects of arraying multiple photodetectors together in order to be used alongside a scintillator, rather than with only one device (as was done in physical experiments). To this end, additional results will be reported for radiation damage and energy deposition in arrays with surface areas of one inch (11 photodetectors per array) and two inches (22 photodetectors per array). The larger effective surface areas of these photodetector arrays also required additional calculations of geometry factor for each: for the one inch array, $\Omega = 7.23\text{x}10^{-3}$ sr; for the two inch array, $\Omega = 1.45\text{x}10^{-2}$ sr.

4.1.3.1 MCNP Radiation Damage Simulation Results

Because of the differences in thickness between Si and organic devices, comparing the radiation damage done to each photodetector is dependent on the flux of particles through each. The fact that MCNP's cell flux tally is weighted by particle track length and the cell's volume means that a one-to-one comparison between radiation damage done to each detector should be understood in the context of particle flux through each detector; additionally, because the implicit calculation of radiation damage in MCNP is done through a tally multiplier modifying the cell flux tally, highly divergent cell flux results between photodetectors could have a significant scaling effect on radiation damage results. As shown in Table 4.1,

Table 4.1: Total particle (neutron + γ-ray) flux results from MCNP simulations of silicon and organic photodiodes in multiple arrangements.

	Particle Flux ($10^6 \frac{\text{neutrons}+\gamma}{\text{cm}^2}$)		
	Single Photodiode	1-in. Array	2-in. Array
Silicon	$2.400 \pm 0.4\%$	$277.2 \pm 0.04\%$	$490.7 \pm 0.02\%$
Organic	$2.397 \pm 0.3\%$	$277.1 \pm 0.03\%$	$490.6 \pm 0.02\%$
Pct. Difference	0.146	0.025	0.014

however, the flux of neutrons and γ-rays through each photodetector is markedly similar, with at most a 0.1% difference between flux values for each. Although MCNP's cell flux tally does not measure particles per unit area (as would be expected given its reported units), the ratio of particle track length to cell volume between photodetectors maintains the expected level of consistency between measured flux values (given the identical geometry factor for silicon and organic devices).

The radiation damage incurred in each of these photodetectors under similar particle fluxes, however, does not appear to follow this pattern. Using displacements per atom as the operative figure of merit for radiation damage, figure 4.5 indicates a rate of damage in silicon nearly two orders of magnitude greater than that of organic devices, suggesting that the organic photodetectors used in this work are significantly more resilient to radiation damage than the silicon devices widely used in radiation detection applications today. Several mitigating factors must be considered before arriving at this conclusion, however.

Within the context of MCNP, the tally multipliers used to convert cell flux data into DPA results differed greatly between photodetector types, as discussed in section 4.1.3.1. The tally multiplier used for silicon was ca. 72 times greater than that of organic devices, which would seem to provide for a substantial portion of the difference in these damage results. However, as is summarized in equation 3.5, physical differences between photodetector materials, such as the greater atomic density and lower displacement threshold energy for silicon (in comparison to carbon, as described in table 3.1), determine this tally multiplier factor, suggesting that this factor reflects silicon's higher propensity for radiation damage

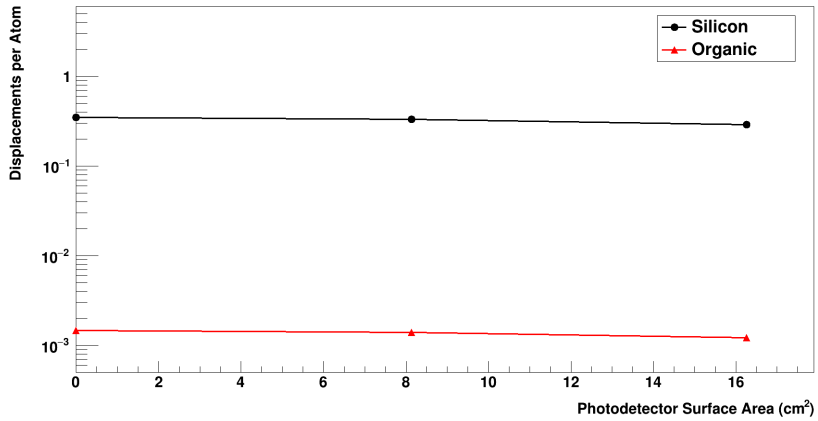

Figure 4.5: Radiation damage induced via atomic collisions by neutrons and γ-rays in silicon and organic photodetectors. Values are reported for individual devices as well as 1-inch and 2-inch arrays. Error bars for results are smaller than symbol size.

(and that it contains implicit physical significance). In addition, the moderation of the AmBe neutron spectrum undergone due to its steel shell and the graphite holder described in section 4.1.2.1 results in many more low energy neutrons reaching the photodetectors, and silicon's damage cross-section (shown in figure 4.2b) is greater throughout this low energy region than in P3HT:ICBA. This cross-section trend is also borne out for γ-ray interactions, as the γ-ray energy spectrum seen by the photodetectors (see figure 4.3b) is a region of comparatively high photoatomic cross-sections for silicon (see figure 4.1).

One other potential explanation for this divergence in radiation damage results stems not from the perspective of interaction probabilities, but the geometric differences between the two types of photodetectors used in this experiment. Though simulated neutron and γ-ray flux results indicated consistency in the number of particles impinging on each device, the reliance of MCNP's tallied flux value on the volume of the detector in question could have some latent effects on the radiation damage calculation. Because each photodetector had similar heights and widths, but the organic devices were significantly thinner than silicon devices, the calculation of $\frac{\text{particle track length}}{\text{cell volume}}$ in MCNP's `F4` tally simplifies to a measure of the particle's track length through the photodetector over the photodetector's thickness.

In this way, detectors of vastly different thicknesses could give very similar results, as these values will scale with one another up to the point where the detector is thick enough to completely stop a particle. Because of this issue, it was determined that the energy deposited in each photodetector could adequately describe whether particles interacted to a similar extent within devices of different sizes.

4.1.3.2 MCNP Energy Deposition Simulation Results

The measurement of energy deposition in MCNP, performed using the `F6` tally, describes a special application of the `F4` tally used to calculate photodetector flux and radiation damage in the previous section. In fact, similar to the radiation damage calculation, energy deposition simulations are simply cell flux tallies with a tally multiplier equal to a material's atomic density divided by its mass density and applied to any reaction that results in "heating" (defined as the energy given to the bulk material in $\frac{\text{MeV}}{\text{collision}}$) [41]. Despite its fundamental reliance on flux measurements, however, its further dependence on collisional energy imparted to a material should account for differences in the number of interactions within materials of differing sizes. This divergence from these flux measurements can be seen in figure 4.6a. While these results differ to a lesser extent than that of radiation damage results shown in figure 4.5, it is clear that organic devices, though with lower atomic and mass densities than in silicon, underwent nearly twice as much energy deposition per unit volume. This phenomenon is likely due to the much larger proportion of collisional energy from neutrons imparted on P3HT:ICBA atoms than in silicon, as is outlined in figure 4.6b. The γ-ray contribution to total energy deposition is roughly equivalent between photodetector types, but the neutron contribution for the organic device is ca. one order of magnitude greater than in silicon. Though neutron cross-sections do play some role in determining the amount of energy that will be imparted by neutrons in a material, of greater significance in this case is a simple difference in neutron kinematic possibilities within each material.

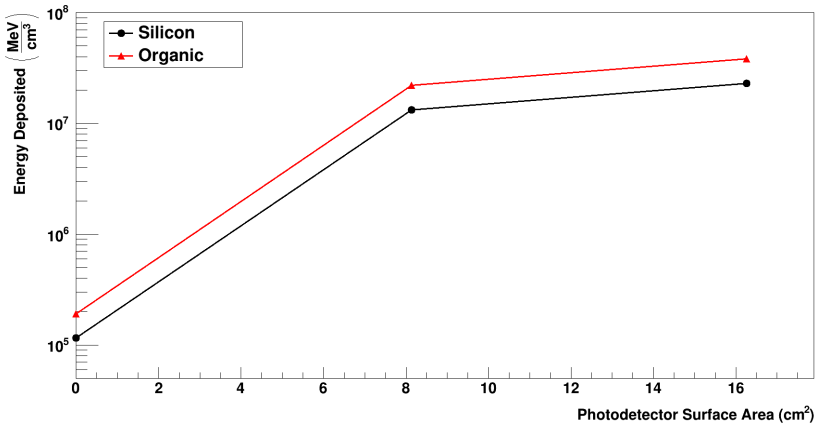

(a) Energy deposited per unit volume by all particles in silicon and organic photodetectors. Values are reported for individual devices as well as 1-inch and 2-inch arrays. Error bars for results are smaller than symbol size.

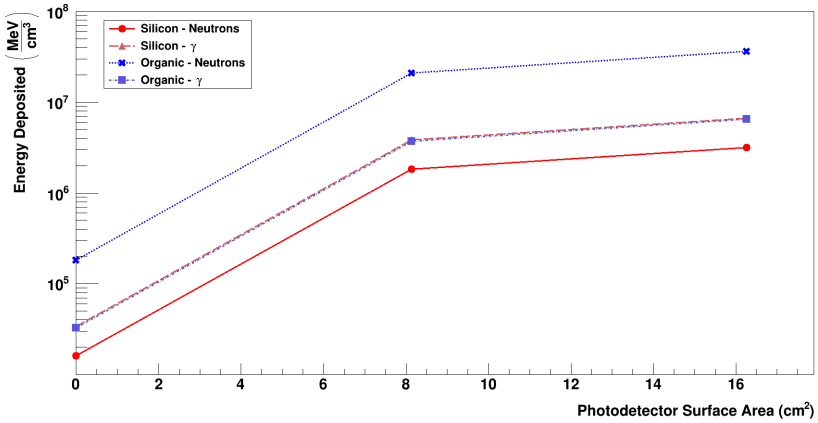

(b) Energy deposited per unit volume by neutrons and γ-rays in silicon and organic photodetectors. Values are reported for individual devices as well as 1-inch and 2-inch arrays. Error bars for results are smaller than symbol size.

Figure 4.6: Energy deposition in silicon and organic photodetectors by all particles and split into neutron and γ-ray contributions.

The primary method by which neutrons impart energy on a material is via direct collision and subsequent elastic recoil with atoms in the material. Thus, the mass of the atoms present in the material plays a significant role in determining the maximum amount of energy that can be transferred to a target atom per interaction in order to conserve momentum. For a head-on collision (in which the incoming neutron and outgoing target atom will move in the same direction), the maximum amount of target atom recoil energy that an incoming neutron can impart is governed through the relation [1]

$$\left.\frac{E_R}{E_n}\right|_{max} = \frac{4A}{(1+A)^2}, \tag{4.6}$$

where E_R is the kinetic energy of the outgoing recoil nucleus, E_n is the energy of the incoming neutron, and A is the ratio of the target nucleus's mass to the mass of a neutron (taken to be 1 amu for simplicity). From this, it is clear that as the mass of the target nucleus increases, $\left.\frac{E_R}{E_n}\right|_{max}$ will tend toward zero; as this nucleus's mass decreases, $\left.\frac{E_R}{E_n}\right|_{max}$ will tend toward unity. In the context of this experiment, the $\left.\frac{E_R}{E_n}\right|_{max}$ for silicon is 0.133, while for P3HT:ICBA (after weighting by atomic fraction to account for its constituents), $\left.\frac{E_R}{E_n}\right|_{max}$ is 0.461. Thus, the greater atomic mass of silicon results in significantly less energy imparted to its constituent nuclei per collision than in the carbon- and hydrogen-rich organic devices. So although silicon's macroscopic neutron scattering cross-section is greater than P3HT:ICBA's across all energies (see figure 4.7b, though note that this higher interaction probability is due to the higher atomic density of silicon, as can be seen in figure 4.7a), the difference in energy transferred per collision more than makes up for this lower interaction probability and results in higher overall energy deposition for the organic device.

As the radiation dose deposited in a material is analogous to energy deposition, it is to be expected that dose results will follow a similar pattern as above (although dose relies on energy per unit mass, rather than per unit volume). Simulation of dose deposition was performed via the use of a tally multiplier for the `F6` tally, and effectively performed a

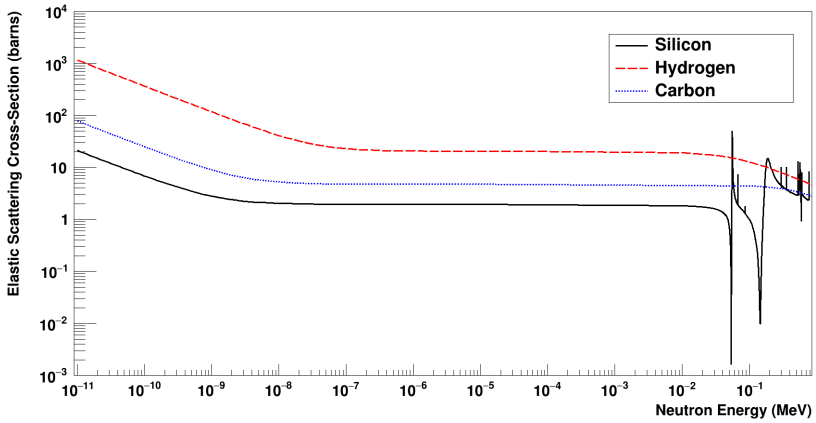

(a) Comparison of microscopic neutron elastic scattering cross-sections of silicon and the carbon and hydrogen components of P3HT:ICBA.

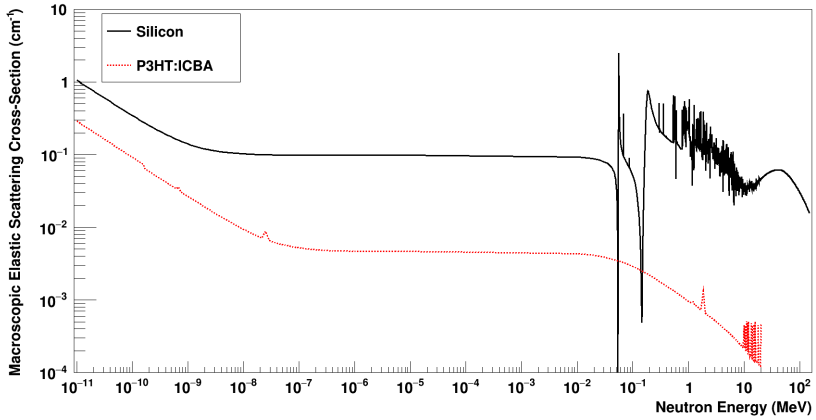

(b) Macroscopic elastic scattering cross-sections for silicon and the organic P3HT:ICBA under neutron irradiation.

Figure 4.7: Neutron elastic scattering cross-section plots for organic and silicon photodetector components.

simple unit conversion to energy deposition data recorded for neutron heating (MT=-4) and total neutron (MT=1) interaction cross-sections [27]. The factor chosen for this tally multiplier was based on the unit conversion

$$1\ \frac{\text{MeV}}{\text{g}} = 1.60\text{x}10^{-6}\frac{\text{ergs}}{\text{g}} = 1.60\text{x}10^{-8}\ \text{rem}$$

As MCNP outputs F6 tally measurements in units of $\frac{\text{MeV}}{\text{g}}$, the tally multiplier used was $1.60\text{x}10^{-8}$. As is shown in figure 4.8, the relationship between dose deposition results for each photodetector type trends closely with that of energy deposition measurements. Of particular note in these measurements is the magnitude of the dose deposited in each detector: neutron and γ-ray dose rates recorded during physical experimentation (at a distance of three feet from the closed collimator box) suggested that the typical dose rate at the distance the photodetectors were placed would be ca. 180 $\frac{\text{mrad}}{\text{hr}}$, translating to a total dose of ca. 3.6 rad (though note that neutron survey meters used for these measurements have significantly larger geometry than photodetectors and were measuring tissue-equivalent dose outside of the confines of the collimator box). Although MCNP simulations predict absorbed dose results slightly below this value, these results suggest that the photodetectors underwent irradiation levels on par with those found in extreme field scenarios. Under such conditions, MCNP simulations indicate that the mixed-field radiation hardness of organic photodetectors exceeds that of silicon devices.

4.1.4 Simulation Error Analysis

4.1.4.1 Statistical Fluctuations due to Monte Carlo Precision

In using Monte Carlo methods to model relatively small-volume geometries (such as with the photodetectors in this work), the issue of uncertainty must play a central role in the analysis of results. Fortunately, MCNP outputs extensive uncertainty information along with tally results, providing the user a high-level understanding of the model's precision (note that the *accuracy* of Monte Carlo methods depends on the model itself and cannot be

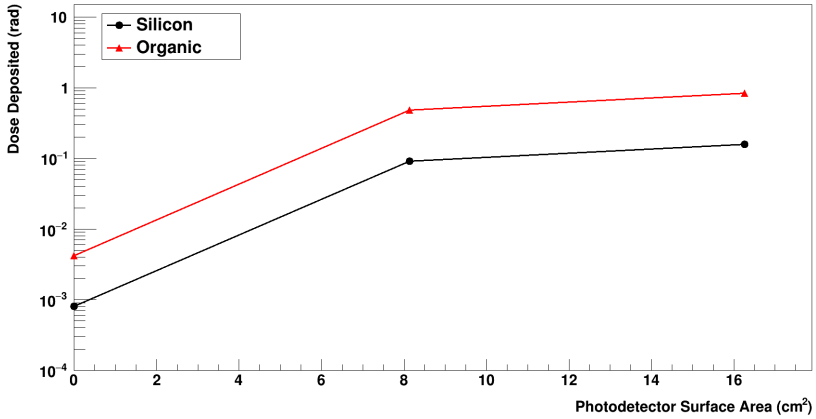

Figure 4.8: Radiation dose deposited by neutrons and γ-rays in silicon and organic photodetectors. Values are reported for individual devices as well as 1-inch and 2-inch arrays. Error bars for results are smaller than symbol size.

quantified directly, while their *precision* is controlled by Monte Carlo parameters and is the uncertainty measurement provided by MCNP). Precision in MCNP is affected by several factors: the number of particle histories run, the type of tally used, choices made to reduce variance in tally results, etc.; utilizing these techniques to arrive at precise results without affecting problem accuracy is of paramount importance.

Within the context of this experiment, obtaining precise results hinged on ensuring that the physics of the problem was maintained while also minimizing the number of particle histories providing no contribution to tally results. Control of this problem's Monte Carlo precision was handled principally through adjustments to variance reduction options and the total number of particle histories run, though in one case other tally types were considered. Due to the size of the photodetectors relative to the size of the problem's geometry as a whole (for instance, the AmBe source's diameter is more than 700 times the thickness of a silicon photodetector, which was the thicker of the devices used in this experiment), the cells encompassing each photodetector could reasonably be collapsed to a single point in space. In doing this, the flux through each photodetector (conventionally measured using an `F4` cell flux tally) could be estimated using a point detector (`F5`) tally; rather than

Table 4.2: Comparison of cell and point detector particle (neutron + γ-ray) flux results from MCNP simulations of silicon and organic photodetectors.

Detector Type	Cell Particle Flux ($10^6 \frac{\text{neutrons}+\gamma}{\text{cm}^2}$)	Point Detector Flux ($10^6 \frac{\text{neutrons}+\gamma}{\text{cm}^2}$)	Percent Difference (%)
Silicon	$2.40 \pm 0.4\%$	$2.41 \pm 1\%$	0.53
Organic	$2.40 \pm 0.3\%$	$2.41 \pm 1\%$	0.43

directly measuring track length of particle through the photoactive region of the detectors, the point detector tally instead measures the particle flux at a point in space as if a particle's next event were to take its trajectory on an uncollided path directly to the detector point [27]. In this way, the `F5` tally provides an upper bound for a surface flux (`F2`) tally at that same point, essentially measuring the probability of any particle in the problem at any event point to pass through the detector's point in space (similarly, the surface flux tally serves as a limiting case for the cell flux tally as the cell becomes infinitely thin) [41]. Particularly for the single photodetector case, similarities between point detector (`F5`) and cell flux (`F4`) tally results would both a) indicate that the choice to collapse the photodetector to a point detector was valid, but also b) suggest that the results from the cell flux tally were reasonable and useful (assuming that the cell flux tally precision was low and that the cell flux did not exceed the limiting case of the point detector flux); results comparing these values are shown in table 4.2. While cell flux for each photodetector type approaches the point detector flux in each case, `F4` results do not exceed `F5` simulations in any case and are in very good agreement in all cases, suggesting that the use of the cell flux tally did not introduce unnecessary uncertainty into these results.

Aside from utilizing tallies of different types, variance reduction methods and changing the number of particle histories to run are the primary techniques by which Monte Carlo precision can be enhanced in MCNP. Variance reduction methods refer to the various built-in MCNP cards that can be employed to increase the likelihood that a given particle history will result in a nonzero history score (or tally contribution). Though MCNP provides several variance reduction options, three were of particular interest for this experiment: cell

importance (IMP), weight windowing (WW), and forced collisions (FCL).

Of these, cell importance definitions are the most commonly used: in the absence of user-defined weight windows, the user will have to define importances for each of the cells present. Cell importance acts as a multiplier for a particular particle's tracks and a divisor of particle weight within that cell; this allows the user to arbitrarily control the "population" of particles within a cell, either by killing the particle upon entrance (with IMP=0) or splitting the particle into multiple tracks (e.g., IMP=3 to create three particle tracks, each with $\frac{1}{3}$ the original particle's weight) [27]. This splitting of particle tracks allows regions that are difficult to sample to be sampled multiple times when particles reach the region. However, for the purposes of this problem, cell importances were set to one for each cell within the problem except outside its bounding sphere, where importance was set to zero (in order to kill wayward particles). This decision to forgo the exploitation of cell importances was made due to the fact that tally fluctuation charts for each photodetector indicated that the probability density functions (PDF) governing history scores were completely sampled even in reasonably short (ca. 3 hour) MCNP runs.

The impetus behind the use of weight windowing methods is similar to that of cell importances: by defining upper and lower particle weight bounds for different regions of a problem (either cell-by-cell or within a user-defined mesh), the user can have each particle be subject to "Russian roulette" (if its particle weight is below the lower weight window bound) or particle track splitting (if its weight is above the upper weight window bound) at each interaction within a given cell/mesh point [41]. This method allows for judicious particle transport, as clearly unimportant particles can be killed off while preferentially sampling particles that travel to regions of interest. However, to ensure computational efficiency, weight windowing techniques are typically paired with source biasing methods to prevent the problem from being bogged down by many successive weight multiplications at each interaction point. In order to avoid the possibility of losing physical fidelity (e.g., through biasing source strength incorrectly, producing an anisotropic source), weight

windowing methods were therefore eliminated from consideration for this simulation.

Finally, the prospect of forcing particle collisions within cells of interest was considered for use in this project. This method simply increases the sampling of particle interactions within cells of interest by artificially inducing a particle collision within the cell and then splitting the particle track into two parts: one uncollided and one collided track (with the uncollided track considered to pass through the entire cell without interacting). The particle weights for each of these tracks are dependent on (and scaled by) the probability of interaction for a particle of that type within the cell's material and volume. Because this variance reduction method is typically used in very thin cells (such as those present in this experiment), the collided particle track often has very low weight, which can result in the collided track being killed before interacting again within the cell of interest (due to particle weight cutoffs) [41]; however, selecting the appropriate forced collision options can mitigate these issues by merely having interactions after the forced collision be sampled normally rather than applying the particle weight cutoff. Though forcing collisions does not have a significant impact on the particle flux measured in a cell, estimates of collision-dependent parameters such as energy deposition (measured via the `F6` tally) can theoretically be improved significantly through its use. The effects of employing forced collisions in the simulations for this experiment are summarized in table 4.3. Unlike the use of point detector tallies in place of cell flux tallies, the impact of utilizing forced collisions to measure energy deposition in each photodetector is clear (while the relative uncertainty for the measurement with forced collisions is significantly higher, relative error for each is $< 10\%$, and runs using forced collisions could establish statistically valid confidence intervals for these measurements at ca. $3\text{x}10^6$ particle histories, which the non-`FCL` was unable to do). Because of the statistical benefits of using forced collisions for this experiment, energy deposition measurements were performed with forced collisions enabled for the photoactive region of each detector type.

The final consideration made regarding the Monte Carlo precision of these simulations

Table 4.3: Comparison of MCNP-simulated energy deposition results from neutrons and γ-rays in silicon and organic photodetectors with and without the forced collisions variance reduction option.

Detector Type	Energy Deposition w/o Forced Collisions ($10^5 \frac{\text{MeV}}{\text{g}}$)	Energy Deposition w/ Forced Collisions ($10^5 \frac{\text{MeV}}{\text{g}}$)	Percent Difference (%)
Silicon	$0.499 \pm 0.7\%$	$0.520 \pm 9\%$	4.02
Organic	$2.14 \pm 0.1\%$	$2.25 \pm 9\%$	4.71

involved the number of particle histories run (selected via the `NPS` card). Because the statistical variance $S_{\bar{x}}^2$ of results obtained via the Monte Carlo method is inherently proportional to $\frac{1}{\sqrt{N}}$ (where N is the number of particle histories run), lowering the statistical spread of data can be computationally expensive in the absence of valid variance reduction techniques. Because the relative error R is related to the variance through the relation [41]

$$R = \frac{S_{\bar{x}}}{\bar{x}}, \tag{4.7}$$

where $\bar{x}$ is the average value of the scores for all histories in the problem and $S_{\bar{x}} = \sqrt{S_{\bar{x}}^2}$ is the standard deviation of the mean, changes in the number of particle histories run for a problem has a direct impact on the Monte Carlo precision. But although minimizing R is an important aspect of ensuring statistical certainty in MCNP tally results, a low R value alone does not guarantee a result's reliability; also of importance is ensuring that the problem's phase space has been adequately sampled over N particle histories.

This is accomplished by measuring the slope of a function $f(x)$ characterizing the tail of the 201 largest history scores for each tally fluctuation chart (TFC) bin for a given tally; this measurement essentially determines whether N can be assumed to be approaching infinity, while also providing a measurement of the level of phase-space sampling present in the problem [41]. If this function falls off at a rate greater than or equal to x^{-3}, then the second history score moment $E(x^2) = \int_{-\infty}^{\infty} x^2 f(x) dx$ is assumed to exist, implying that the chosen N can be thought of as approaching infinity and that $f(x)$ has converged. Within the context of MCNP, the slope of $f(x)$ is measured throughout the run based on a

continuously-updated list of the 201 largest history scores for each TFC bin on a log-log basis. Therefore, a slope greater than three indicates that $f(x)$ is falling off at a rate greater than that of x^{-3}; this value is reported as one of the ten statistical checks performed by MCNP during the run. As this slope depends entirely on how well-sampled the problem's phase-space is, it is affected most prominently by the number of particle histories run and the amount of phase-space sampling variance reduction is performed. With the availability of reasonable variance reduction options limited by the physical integrity of the simulation, however, the number of particle histories was considered to be the adjustable parameter for this statistical test.

Though the NPS values required for SiPD and OPD simulations to achieve acceptable R <0.10 uncertainty values were reasonable (NPS=1.28x10^6 for SiPD runs and NPS=1.41x10^6 for OPD runs), reaching $f(x)$ tail slopes above three required significantly larger NPS values (this resulted in the extremely low R values found in the results for these simulations throughout this chapter). As shown in figure 4.9, more than 10^8 particle histories were required in order to adequately sample the phase spaces of both SiPD and OPD simulations (photon flux tallies were chosen to quantify this due to the greater quantity of sampled neutrons and the lack of variance reduction options benefiting flux tallies). As a result, for the purposes of these simulations, 5x10^8 particle histories were run for SiPD simulations and 1x10^9 histories were run in OPD simulations.

4.2 Experimental Results

As the primary consequences of radiation damage in photodetectors are a breakdown in their ability to detect light signals and an increase in their leakage current, much of the data obtained during experimentation was based on the electronic performance of the devices. Measurements of leakage current were performed before, during, and after irradiation (each for ca. 20 hours), in each case measuring the change in leakage current as applied voltage was varied between -1.5 and 1.5 V every five minutes (such that each voltage increment was

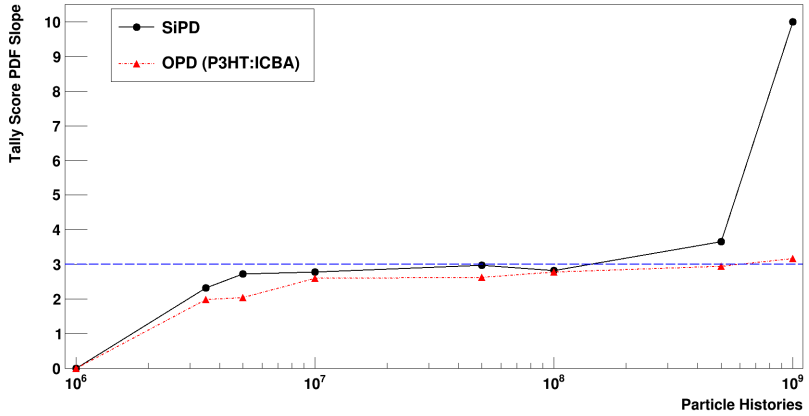

Figure 4.9: Statistical measure of the probability density function tail slope for photon flux tallies for SiPD and OPD simulations at various NPS values. Statistically valid confidence intervals can be formed if the slope exceeds 3 (shown as the dashed line in the figure).

re-measured once every five minutes). In the pre-irradiation case (shown in figure 4.10), organic devices displayed considerably lower leakage current under positive biases while maintaining parity with silicon in the negative bias regime. This difference in leakage current at positive voltages suggests that even outside of field scenarios, organic photodetectors could be used to provide lower noise levels than silicon devices for the counting of very weak scintillation signals from radiation detectors.

Measurements of leakage current during irradiation offered the chance to see the real-time change in photodetector performance under conditions similar to that of a field scenario. As with measurements taken prior to irradiation, bias voltage was varied between -1.5 and 1.5 V over a period of five minutes and leakage current was recorded at each voltage increment. The resulting change in leakage current over the full 20 hour period, shown for the organic device in figure 4.11, indicates a noticeable change in the performance of the photodetector under prolonged exposure to such a high-flux source. Most telling is the rise in leakage current under zero bias, indicating that even in the absence of applied voltage or external light sources, the current across the photoactive layer increases to a small extent as the device is damaged by radiation.

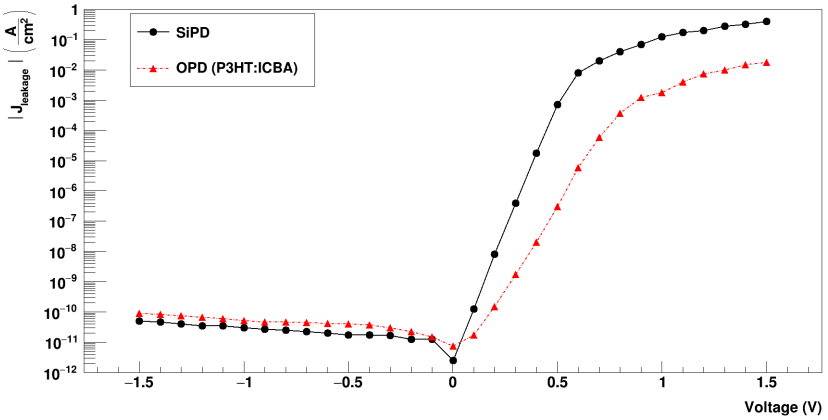

Figure 4.10: Experimental leakage current density results for silicon and organic photodetectors as a function of applied voltage prior to irradiation. Error bars for results are smaller than symbol size.

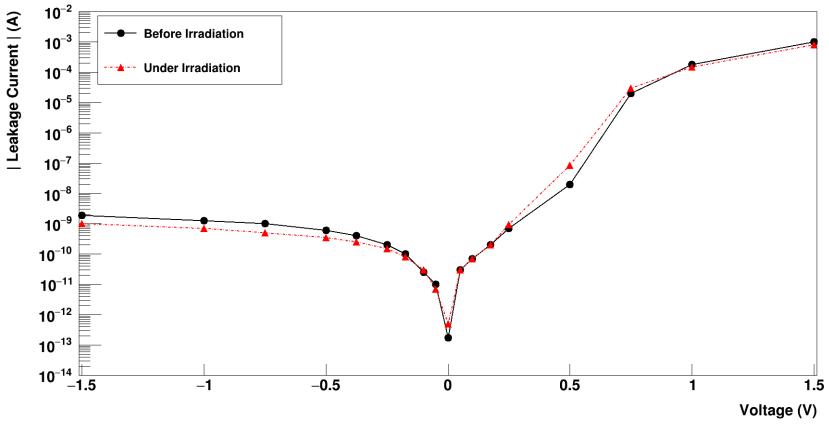

Figure 4.11: Experimental leakage current results for a P3HT:ICBA organic photodetector as a function of applied voltage just prior to and just after a 20-hour exposure to a mixed-field neutron/γ-ray source. Error bars for results are smaller than symbol size.

Though similar trials were attempted using silicon devices for comparison purposes, the software developed to perform these measurements was incompatible with devices not developed at Georgia Tech. Fortunately, this subject is an area of active research and results regarding the resilience of silicon detectors to irradiation abound. Typical literature results indicate that SiPDs under irradiation see their leakage current rise to ca. 0.15 μA under a bias voltage of 0V, rising to ca. 1 mA with an applied bias voltage of 1.5V [26, 42]. Comparing these results against figure 4.11, silicon devices appear to provide a similar level of performance when biased during irradiation while performing significantly worse when unbiased. With leakage current values varying between 1 μA and 1 mA in silicon, the weak signals produced by scintillation light would likely be unable to exceed these thresholds. Meanwhile, OPDs are capable of maintaining leakage currents in the range of ca. 1 pA - 1 nA under a similar level of irradiation, and irradiation induces only an average factor of 2 difference in leakage current for OPDs (compared to an average factor of ca. 6.5 in SiPDs [43]). These results indicate that irradiation has a significantly greater impact on the performance of SiPDs compared to OPDs, and appears to support the radiation damage results obtained in MCNP simulations.

CHAPTER 5
CONCLUSION

In this work, the resilience to neutron and γ-ray irradiation of silicon photodetectors (quantified by simulated radiation damage measurements and experimental leakage current results) was compared to that of organic photodetectors developed at Georgia Tech. In collaboration with the Center for Organic Photonics, an experimental design was developed in order to measure the change in leakage current through these devices while under irradiation by a high-activity americium-beryllium radiation source. Additionally, MCNP simulations were performed to study the radiation damage induced in each device under such an experiment, which required the modification of ENDF-B/VIII neutron and photoatomic cross-section libraries using the NJOY code. The goal of this work was to quantify and compare the effects of a high-fluence, mixed-field radiation source on the electronic performance of organic photodetectors as a method of determining their effectiveness while employed in a field scenario as light collection devices alongside scintillation detectors. Experimental results for the leakage current in Georgia Tech's organic photodetectors (compared to readily-available silicon photodetector data in literature) suggest that organics experience a roughly twofold change in leakage current due to irradiation, while silicon devices show leakage currents ca. 6.5 times higher while under irradiation. MCNP measurements indicate a similar trend; in silicon, irradiation resulted in rates of atomic displacement ca. two orders of magnitude greater than in equivalent organic devices, even while experiencing radiation dose rates nearly an order of magnitude in excess of silicon photodetectors. These results are encouraging for the future of organic photodetectors as an alternative to industry-standard silicon devices, particularly in applications in which high neutron and γ-ray fluences are anticipated.

CHAPTER 6

FUTURE WORK

As a natural extension to this work, radiation detection experiments utilizing organic photodetectors alongside scintillation detectors will be performed in order to determine their light collection efficiency relative to silicon detectors (experiments that will be performed both pre- and post-irradiation). In addition, the self-annealing rate (or the rate at which displaced atoms relax into a new structure, allowing the photodetector to recover some of its performance) for these detectors will be studied in order to quantify the recoverability of this radiation damage. Performing these measurements will be crucial in determining the utility of organic photodetectors for the specific application of scintillation counting in high-fluence environments.

Appendices

APPENDIX A

SAMPLE MCNP INPUTS

A.1 Silicon Photodiode Irradiation Input

This input describes the irradiation of a single silicon photodiode with dimensions equal to that of a Hamamatsu S1133 device. The system consists of the photodiode, the AmBe neutron/γ source, the collimator box, the graphite AmBe source holder, and the floor of the neutron generator vault, contained in an air sphere.

```
1  Silicon Photodiode with AmBe inside Collimator Box
2  c
3  c Jake Inman, Georgia Institute of Technology
4  c Note: all units given per source particle
5  c
6  c                                        CELL CARDS
7  c
8  c Collimator Box Cells
9  c
10 c Graphite AmBe holder
11 1 4 -1.7 (4 -5 12 -13 18 -19 123):(103 -123 18 -104)
12 c
13 c Outer concrete layer, all but lid
14 2 2 -2.3 1 -8 9 -15 56 -20 (-2:7:-10:14:-17)
15 c
16 c Inner steel layer, all but lid
17 3 3 -8.0 2 -7 10 -14 17 -20 (-3:6:-11:13:-18)
18 c
19 c Inner concrete layer, lid
20 4 2 -2.3 2 -7 10 -14 20 -21
21 c
22 c Outer steel layer, lid
23 5 3 -8.0 1 -8 9 -15 20 -22 (-2:7:-10:14:21)
24 c
25 c Silicon photodiode
26 6 6 -2.3296 31 -32 33 -12 35 -36
27 c
28 c Air inside collimator box
29 7 1 -0.001205 (3 -4 11 -13 18 -20):(5 -6 11 -13 18 -20):
30       (4 -31 11 -12 18 -20):(32 -5 11 -12 18 -20):
31       (31 -32 11 -33 18 -20):(4 -5 33 -13 19 -20):
32       (31 -32 33 -12 18 -35):(31 -32 33 -12 36 -19):
33       (103 -123 104 -19)
34 c
35 c AmBe Cells
36 c
37 c AmBe material
38 101 5 -1.214 -101
```

```
c
c Air gap
102 1 -0.001205 101 -102
c
c Steel shell around AmBe
103 3 -8.0 102 -103
c
c Room Cells
c
c Floor (concrete)
50 2 -2.3 51 -52 53 -54 55 -56
c
c Air sphere
200 1 -0.001205 -200 ((-51:52:-53:54:-55:56)
      (-1:8:-9:15:-56:22))
c
c Problem Enclosure
c Graveyard (void)
999 0 200

c                                   SURFACE CARDS
c
c                    Collimator Box and Graphite Block Surfaces
c
c                                       X-PLANES
c
c Leading concrete edge, side of box opposite hinges
1 px -25.7175
c
c Leading steel edge
2 px -19.05
c
c Box interior edge
3 px -15.24
c
c Leading edge of graphite block
4 px -10.795
c
c Trailing edge of graphite block
5 px 10.4775
c
c Box interior edge
6 px 14.9225
c
c Trailing steel edge
7 px 17.145
c
c Trailing concrete edge, side of box with hinges
8 px 25.7175
c
c                                       Y-PLANES
c
c Leading concrete edge, side of box with collimator hole
9 py -28.8925
c
c Leading steel edge
10 py -22.86
c
c Box interior edge
11 py -18.7325
c
```

```
c Leading edge of graphite block, shared with trailing edge of SiPD
12 py 7.62
c
c Box interior edge, shared with trailing edge of graphite block
13 py 17.4625
c
c Trailing steel edge
14 py 22.5425
c
c Trailing concrete edge, side of box opposite collimator hole
15 py 28.8925
c
c                                   Z-PLANES
c
c Leading steel edge of box
17 pz -18.0975
c
c Box interior edge, shared with Leading edge of graphite block
18 pz -12.065
c
c Trailing edge of graphite block
19 pz -2.2225
c
c Box interior edge
20 pz 17.4625
c
c Trailing concrete edge
21 pz 23.6583
c
c Trailing steel edge, top of box
22 pz 25.0825
c
c                              NON-PLANAR SURFACES
c
c Air cylinder in graphite block for placing AmBe
123 c/z -0.16275 12.5413 3.048
c
c                                 SiPD Surfaces
c
c Leading x edge of SiPD
31 px -0.27875
c
c Trailing x edge of SiPD
32 px -0.03875
c
c Leading y edge of SiPD
33 py 7.613
c
c Trailing y edge of SiPD is shared with graphite block; see surface 12
c 34 py 7.62 $ as a placeholder
c
c Leading z edge of SiPD
35 pz -6.9345
c
c Trailing z edge of SiPD
36 pz -6.6545
c
c
c                                 Floor Surfaces
c
c Leading x floor boundary
```

```
51 px -100
c
c Trailing x floor boundary
52 px 100
c
c Leading y floor boundary
53 py -100
c
c Trailing y floor boundary
54 py 100
c
c Leading z floor boundary
55 pz -125.0825
c
c Trailing z floor boundary
56 pz -25.0825
c
c                                   AmBe Surfaces
c
c AmBe material inside steel casing
101 s -0.16275 12.5413 -6.7945 2.7305
c
c Inner edge of steel casing
102 s -0.16275 12.5413 -6.7945 2.73051
c
c Outer edge of steel casing
103 s -0.16275 12.5413 -6.7945 3.048
c
c Plane of middle of AmBe sphere
104 pz -6.7945
c
c                             Problem Bounding Surfaces
c
c Air sphere surrounding geometry
200 so 200

c                                   DATA CARDS
c
c                                MATERIAL SPECIFICATIONS
c
c Dry air, 0.001205 g/cc
m1 6000 0.000150 7014 0.784431 8016 0.210784 18000 0.004671
c
c Concrete, 2.3 g/cc from NIST
m2 1001 0.305330 6000 0.002880 8016 0.500407 11023 0.009212
      12000 0.000725 13027 0.010298 14000 0.151042
      19000 0.003578 20000 0.014924 26000 0.001605
c
c Stainless steel 304, 8.0 g/cc 304 L
m3 6000 0.000687 14000 0.009793 15031 0.000408 16000 0.000257
      24000 0.201015 25055 0.010013 26000 0.684101 28000 0.093725
c
c Graphite, 1.7 g/cc
m4 6000 1.000000
c
c Other Materials
c
c AmBe
c Americium beryllium, 1.214 g/cc
m5 95241.66c -0.200000 4009.62c -0.800000
c
```

```
c Silicon photodiode
c Silicon, ~2.3296 g/cc
m6 14028 1.000000
c
c
c                                PHYSICS SPECIFICATIONS
c
c
c Problem Mode
c Track neutrons and photons only
mode n p
c
c Cell Importances
c Particle weight of 1 for every cell except graveyard
imp:n,p 1 11r 0
c
c
c                            CELL AND SURFACE SPECIFICATIONS
c
c Entered Tally Cell Volumes
c Calculated volumes for collimator box, air inside collimator box, SiPD,
c and air outside collimator box
vol 1847.64 4j 4.704e-4 30388.36 4j 32361222.656291128 j
c
c
c                           VARIANCE REDUCTION SPECIFICATIONS
c
c Forced collisions in SiPD (cell 6)
fcl:n 5j -1 7j
fcl:p 5j -1 7j
c
c                                SOURCE SPECIFICATIONS
c
c   Neutron source, AmBe neutron energy spectrum, distributed radially about
c                            center of AmBe material cell
sdef par d1 erg fpar d2  rad d5  cel 101 pos -0.16275 12.5413 -6.7945
c
si1 l 1 2
c
sp1 0.635593 0.364407
c
sc1 0.537:1 gamma/neutron emission probabilities
c
ds2 s 3 4
c
sc2 dependent on particle distribution; neutrons: 3, gammas: 4
c
si3 h 4.14e-7 0.11 0.33 0.54 0.75 0.97 1.18 1.40 1.61 1.82 2.04
      2.25 2.47 2.68 2.90 3.11 3.32 3.54 3.75 3.97 4.18 4.39 4.61
      4.82 5.04 5.25 5.47 5.68 5.89 6.11 6.32 6.54 6.75 6.96 7.18
      7.39 7.61 7.82 8.03 8.25 8.46 8.68 8.89 9.11 9.32 9.53 9.75
      9.96 10.18 10.39 10.6 10.82 11.03
c
sp3 d 0 0.0144 0.0334 0.0313 0.0281 0.025 0.0214 0.0198 0.0175
      0.0192 0.0222 0.0215 0.0225 0.0228 0.0295 0.0356 0.0368
      0.0346 0.0307 0.0300 0.0269 0.0286 0.0318 0.0307 0.0333 0.0304
      0.0274 0.0233 0.0206 0.0181 0.0177 0.0204 0.0183 0.0163
      0.0168 0.0168 0.0188 0.0184 0.0169 0.0143 0.0097 0.0065
      0.0043 0.0037 0.0038 0.0051 0.0062 0.0055 0.0047 0.0037
      0.0028 0.0015 0.0004
c
```

```
sc3 Neutron Energy Distribution - ISO 8529 AmBe neutron energy spectrum;
     Neutrons emitted due to 9Be + alpha rxn
c
si4 l 4.438
c
sp4 d 1
c
sc4 12C excited state gamma due to 9Be(alpha,n) rxn
c
si5 0 2.7305
c
sp5 -21 2
c
sc5 Power law radial probability distribution: p(x)=c|x|^2
c
c
c                                TALLY SPECIFICATIONS
c
c Standard F Tallies
c
c Neutron Tallies
c
f604:n 6
fc604 neutron flux through SiPD cell
c
f614:n 6
fc614 neutron-induced DPA in Si photodiode
fm614 1002.8845968 6 444 $ converts F4 tally to DPA for silicon
c
f606:n 6
fc606 neutron energy deposition in SiPD
c
f616:n 6
fc616 neutron dose deposited in SiPD
fm616 1.602e-8 6 -1 -4 $ converts F6 tally to dose tally (rads) for silicon
c
c Photon Tallies
c
f624:p 6
fc624 photon flux through SiPD cell
c
f626:p 6
fc626 photon energy deposition in SiPD
c
f636:p 6
fc636 photon dose deposited in SiPD
fm636 1.602e-8 6 -5 -6 $ converts F6 tally to dose tally (rads) for silicon
c
c Mesh Tallies
c
c FMESH - DPA and F4 mesh tallies
c
fmesh634:n geom xyz origin -0.27875 7.613 -6.9345
     imesh -0.03875 jmesh 7.62 kmesh -6.6545
     iints 1 jints 10 kints 1
     out cf
fc634 neutron flux in SiPD, meshed
c
fmesh644:n geom xyz origin -0.27875 7.613 -6.9345
     imesh -0.03875 jmesh 7.62 kmesh -6.6545
     iints 1 jints 10 kints 1
```

```
344       out cf
345 fc644 neutron-induced DPA in SiPD, meshed
346 fm644 1002.8845968 6 444
347 c
348 fmesh654:p geom xyz origin -0.27875 7.613 -6.9345
349       imesh -0.03875 jmesh 7.62 kmesh -6.6545
350       iints 1 jints 10 kints 1
351       out cf
352 fc654 photon flux in SiPD, meshed
353 c
354 c TMESH - F6 and dose mesh tallies
355 c
356 tmesh
357 c
358 c c neutron flux through SiPD - check for FMESH tally 654
359 rmesh601:n flux
360 cora601 -0.27875 -0.03875
361 corb601 7.613 9i 7.62
362 corc601 -6.9345 -6.6545
363 c
364 c neutron DPA in SiPD - check for FMESH tally 664
365 rmesh611:n flux
366 cora611 -0.27875 -0.03875
367 corb611 7.613 9i 7.62
368 corc611 -6.9345 -6.6545
369 c
370 c photon flux through SiPD - check for FMESH tally 674
371 rmesh621:p flux
372 cora621 -0.27875 -0.03875
373 corb621 7.613 9i 7.62
374 corc621 -6.9345 -6.6545
375 c
376 c neutron energy deposition in SiPD
377 rmesh631:n pedep
378 cora631 -0.27875 -0.03875
379 corb631 7.613 9i 7.62
380 corc631 -6.9345 -6.6545
381 c
382 c neutron dose delivered to SiPD (rad)
383 rmesh641:n pedep
384 cora641 -0.27875 -0.03875
385 corb641 7.613 9i 7.62
386 corc641 -6.9345 -6.6545
387 c
388 c photon energy deposition in SiPD
389 rmesh651:p pedep
390 cora651 -0.27875 -0.03875
391 corb651 7.613 9i 7.62
392 corc651 -6.9345 -6.6545
393 c
394 c photon dose delivered to SiPD (rad)
395 rmesh661:p pedep
396 cora661 -0.27875 -0.03875
397 corb661 7.613 9i 7.62
398 corc661 -6.9345 -6.6545
399 c
400 c direct measurement of neutron dose delivered to SiPD (rem/hr)
401 rmesh671:n dose
402 cora671 -0.27875 -0.03875
403 corb671 7.613 9i 7.62
404 corc671 -6.9345 -6.6545
```

```
405 c
406 c direct measurement of photon dose delivered to SiPD (rem/hr)
407 rmesh681:p dose
408 cora681 -0.27875 -0.03875
409 corb681 7.613 9i 7.62
410 corc681 -6.9345 -6.6545
411 c
412 endmd
413 c
414 c Mesh tally multipliers
415 fm611 1002.8845968 6 444 $ converts flux tally to DPA for neutrons
416 fm641 1.602e-8 6 -1 -4 $ converts energy deposition to dose for neutrons (rad)
417 fm661 1.602e-8 6 -5 -6 $ converts energy deposition to dose for photons (rad)
418 c
419 c
420 c                          PROBLEM TERMINATION SPECIFICATIONS
421 c
422 nps 5e8
423 c in 20 hour run: 8.57e12 neutrons, 4.91601e12 gammas
```

A.2 Organic Photodiode Irradiation Input

This input describes the irradiation of a single organic photodiode with dimensions equal to that of the OPDs developed by COPE for this project. The system consists of the photodiode, the AmBe neutron/γ source, the collimator box, the graphite AmBe source holder, and the floor of the neutron generator vault, contained in an air sphere.

```
1  Organic Photodiode Irradiation with AmBe inside Collimator Box
2  c
3  c Jake Inman, Georgia Institute of Technology
4  c Note: all units given per source particle
5  c
6  c                                    CELL CARDS
7  c
8  c Collimator Box Cells
9  c
10 c Graphite AmBe holder
11 1 4 -1.7 (4 -5 12 -13 18 -19 123):(103 -123 18 -104)
12 c
13 c Outer concrete layer, all but lid
14 2 2 -2.3 1 -8 9 -15 56 -20 (-2:7:-10:14:-17)
15 c
16 c Inner steel layer, all but lid
17 3 3 -8.0 2 -7 10 -14 17 -20 (-3:6:-11:13:-18)
18 c
19 c Inner concrete layer, lid
20 4 2 -2.3 2 -7 10 -14 20 -21
21 c
22 c Outer steel layer, lid
23 5 3 -8.0 1 -8 9 -15 20 -22 (-2:7:-10:14:21)
24 c
25 c Organic Photodiode Cells
```

```
c Ag layer
6 10 -10.5 31 -32 33 -34 40 -41
c
c MoO3 layer
7 8 -4.69 31 -32 34 -35 40 -41
c
c P3HT:ICBA photoactive layer
8 9 -1.1 31 -32 35 -36 40 -41
c
c MoO3 layer
9 8 -4.69 31 -32 36 -37 40 -41
c
c ITO layer
10 7 -7.14 31 -32 37 -38 40 -41
c
c Glass layer
11 6 -2.4 31 -32 38 -12 40 -41
c
c Air inside collimator box
12 1 -0.001205 (3 -4 11 -13 18 -20):(5 -6 11 -13 18 -20):
      (4 -31 11 -12 18 -20):(32 -5 11 -12 18 -20):
      (31 -32 11 -33 18 -20):(4 -5 33 -13 19 -20):
      (31 -32 33 -12 18 -40):(31 -32 33 -12 41 -19):
      (103 -123 104 -19)
c
c AmBe Cells
c
c AmBe material
101 5 -1.214 -101
c
c Air gap
102 1 -0.001205 101 -102
c
c Steel shell around AmBe
103 3 -8.0 102 -103
c
c Room Cells
c
c Floor (concrete)
50 2 -2.3 51 -52 53 -54 55 -56
c
c Air sphere
200 1 -0.001205 -200 ((-51:52:-53:54:-55:56)
      (-1:8:-9:15:-56:22))
c
c Graveyard (void)
999 0 200

c                                   SURFACE CARDS
c
c                    Collimator Box and Graphite Block Surfaces
c
c                                     X-PLANES
c
c Leading concrete edge, side of box opposite hinges
1 px -25.7175
c
c Leading steel edge
2 px -19.05
c
c Box interior edge
```

```
3 px -15.24
c
c Leading edge of graphite block
4 px -10.795
c
c Trailing edge of graphite block
5 px 10.4775
c
c Box interior edge
6 px 14.9225
c
c Trailing steel edge
7 px 17.145
c
c Trailing concrete edge, side of box with hinges
8 px 25.7175
c
c                                    Y-PLANES
c
c Leading concrete edge, side of box with collimator hole
9 py -28.8925
c
c Leading steel edge
10 py -22.86
c
c Box interior edge
11 py -18.7325
c
c Trailing edge of glass layer, shared with leading edge of graphite block
12 py 7.62
c
c Box interior edge, shared with trailing edge of graphite block
13 py 17.4625
c
c Trailing steel edge
14 py 22.5425
c
c Trailing concrete edge, side of box opposite collimator hole
15 py 28.8925
c
c                                    Z-PLANES
c
c Leading steel edge of box
17 pz -18.0975
c
c Box interior edge, shared with leading edge of graphite block
18 pz -12.065
c
c Trailing edge of graphite block
19 pz -2.2225
c
c Box interior edge
20 pz 17.4625
c
c Trailing concrete edge
21 pz 23.6583
c
c Trailing steel edge, top of box
22 pz 25.0825
c
c                              NON-PLANAR SURFACES
```

```
c
c Air cylinder in graphite block for placing AmBe
123 c/z -0.16275 12.5413 3.048
c
c
c                                   OPD Surfaces
c
c Leading x edge of OPD
31 px -0.27875
c
c Trailing x edge of OPD
32 px -0.03875
c
c Leading y edge of silver electrode layer
33 py 7.6199992
c
c Leading y edge of MoO3 layer
34 py 7.61999935
c
c Leading y edge of photoactive layer
35 py 7.61999936
c
c Leading y edge of MoO3 layer
36 py 7.61999987
c
c Leading y edge of ITO layer
37 py 7.61999988
c
c Leading y edge of glass layer
38 py 7.61999994
c
c Trailing y edge of glass layer shared with graphite block; see surface 12
c
c Leading z edge of OPD
40 pz -6.9345
c
c Trailing z edge of OPD
41 pz -6.6545
c
c                                  Floor Surfaces
c
c Leading x floor boundary
51 px -100
c
c Trailing x floor boundary
52 px 100
c
c Leading y floor boundary
53 py -100
c
c Trailing y floor boundary
54 py 100
c
c Leading z floor boundary
55 pz -125.0825
c
c Trailing z floor boundary
56 pz -25.0825
c
c                                   AmBe Surfaces
c
```

```
c AmBe material inside casing
101 s -0.16275 12.5413 -6.7945 2.7305
c
c Inner edge of steel casing
102 s -0.16275 12.5413 -6.7945 2.73051
c
c Outer edge of steel casing
103 s -0.16275 12.5413 -6.7945 3.048
c
c Plane of middle of AmBe sphere
104 pz -6.7945
c
c                              Problem Bounding Surfaces
c
c Air sphere surrounding geometry
200 so 200

c                                      DATA CARDS
c
c                                  MATERIAL SPECIFICATIONS
c
c Dry air, 0.001205 g/cc
m1 6000 0.000150 7014 0.784431 8016 0.210784 18000 0.004671
c
c Concrete, 2.3 g/cc from NIST
m2 1001 0.305330 6000 0.002880 8016 0.500407 11023 0.009212
      12000 0.000725 13027 0.010298 14000 0.151042
      19000 0.003578 20000 0.014924 26000 0.001605
c
c Stainless steel 304, 8.0 g/cc 304 L
m3 6000 0.000687 14000 0.009793 15031 0.000408 16000 0.000257
      24000 0.201015 25055 0.010013 26000 0.684101 28000 0.093725
c
c Graphite, 1.7 g/cc
m4 6000 1.000000
c
c Other Materials
c
c AmBe
c Americium beryllium, 1.214 g/cc
m5 95241.66c -0.200000 4009.62c -0.800000
c
c Organic photodiode
c Plate glass, 2.4 g/cc
m6 8016 0.603858 11023 0.088145 14000 0.251791 20000 0.056205
c
c ITO, 7.14 g/cc
m7 8016 0.625 49000 0.25 50000 0.125
c
c Molybdenum trioxide, 4.69 g/cc
m8 8016 0.75 42000 0.25
c
c P3HT:ICBA, 1.1 g/cc
m9 1001 0.38964 6000 0.58784 16000 0.02252
c
c Silver, 10.5 g/cc
m10 47000 1.000000
c
c
c                                  PHYSICS SPECIFICATIONS
c
```

```
c
c Problem Mode
c Track neutrons and photons only
mode n p
c
c Cell Importances
c Particle weight of 1 for every cell except graveyard
imp:n,p 1 16r 0
c
c
c                          CELL AND SURFACE SPECIFICATIONS
c
c Entered Tally Cell Volumes
c Calculated volumes for collimator box, air inside collimator box, OPD,
c and air outside collimator box
vol 1847.6363159531 6j 3.4272e-8 3j 30388.467389856 4j 32361222.656291128 j
c
c
c                         VARIANCE REDUCTION SPECIFICATIONS
c
c Forced collisions in OPD photoactive cell only (cell 8)
fcl:n 7j -1 10j
fcl:p 7j -1 10j
c
c Forced collisions in all OPD cells
c fcl:n 5j -1 5r 7j
c fcl:p 5j -1 5r 7j
c
c                                SOURCE SPECIFICATIONS
c
c          AmBe neutron+gamma source, distributed radially about
c                           center of AmBe material cell
sdef par d1 erg fpar d2  rad d5  cel 101 pos -0.16275 12.5413 -6.7945
c
si1 l 1 2
c
sp1 0.635593 0.364407
c
sc1 0.537:1 gamma/neutron emission probabilities
c
ds2 s 3 4
c
sc2 dependent on particle distribution; neutrons: 3, gammas: 4
c
si3 h 4.14e-7 0.11 0.33 0.54 0.75 0.97 1.18 1.40 1.61 1.82 2.04
      2.25 2.47 2.68 2.90 3.11 3.32 3.54 3.75 3.97 4.18 4.39 4.61
      4.82 5.04 5.25 5.47 5.68 5.89 6.11 6.32 6.54 6.75 6.96 7.18
      7.39 7.61 7.82 8.03 8.25 8.46 8.68 8.89 9.11 9.32 9.53 9.75
      9.96 10.18 10.39 10.6 10.82 11.03
c
sp3 d 0 0.0144 0.0334 0.0313 0.0281 0.025 0.0214 0.0198 0.0175
      0.0192 0.0222 0.0215 0.0225 0.0228 0.0295 0.0356 0.0368
      0.0346 0.0307 0.0300 0.0269 0.0286 0.0318 0.0307 0.0333 0.0304
      0.0274 0.0233 0.0206 0.0181 0.0177 0.0204 0.0183 0.0163
      0.0168 0.0168 0.0188 0.0184 0.0169 0.0143 0.0097 0.0065
      0.0043 0.0037 0.0038 0.0051 0.0062 0.0055 0.0047 0.0037
      0.0028 0.0015 0.0004
c
sc3 Neutron Energy Distribution - ISO 8529 AmBe neutron energy spectrum;
      Neutrons emitted due to 9Be + alpha rxn
c
```

```
si4 l 4.438
c
sp4 d 1
c
sc4 12C excited state gamma due to 9Be(alpha,n) rxn
c
si5 0 2.7305
c
sp5 -21 2
c
sc5 Power law radial probability distribution: p(x)=c|x|^2
c
c
c                                TALLY SPECIFICATIONS
c
c Standard F Tallies
c
c Neutron Tallies
c
f804:n 8
fc804 neutron flux through OPD cell
c
f814:n 8
fc814 neutron-induced DPA in organic photodiode
fm814 13.9018 9 444 $ converts F4 tally to DPA for P3HT:ICBA
c
f806:n 8
fc806 neutron energy deposition in OPD
c
f816:n 8
fc816 neutron dose deposited in OPD
fm816 1.602e-8 9 -1 -4 $ converts F6 tally to dose tally (rads) for P3HT:ICBA
c
c Photon Tallies
c
f824:p 8
fc824 photon flux through OPD cell
c
f826:p 8
fc826 photon energy deposition in SiPD
c
f836:p 8
fc836 photon dose deposited in SiPD
fm836 1.602e-8 6 -5 -6 $ converts F6 tally to dose tally (rads) for silicon
c
c Mesh Tallies
c
c FMESH - DPA and F4 mesh tallies
c
fmesh834:n geom xyz origin -0.27875 7.61999936 -6.9345
      imesh -0.03875 jmesh 7.619999987 kmesh -6.6545
      iints 1 jints 10 kints 1
      out cf
fc834 neutron flux in OPD, meshed
c
fmesh844:n geom xyz origin -0.27875 7.61999936 -6.9345
      imesh -0.03875 jmesh 7.619999987 kmesh -6.6545
      iints 1 jints 10 kints 1
      out cf
fc844 neutron-induced DPA in OPD, meshed
fm844 13.9018 9 444
```

```
c
fmesh854:p geom xyz origin -0.27875 7.61999936 -6.9345
     imesh -0.03875 jmesh 7.619999987 kmesh -6.6545
     iints 1 jints 10 kints 1
     out cf
fc854 photon flux in OPD, meshed
c
c TMESH - F6 and dose mesh tallies
c
tmesh
c
c neutron flux through OPD - check for FMESH tally 854
rmesh801:n flux
cora801 -0.27875 -0.03875
corb801 7.61999936 9i 7.61999987
corc801 -6.9345 -6.6545
c
c neutron DPA in OPD - check for FMESH tally 864
rmesh811:n flux
cora811 -0.27875 -0.03875
corb811 7.61999936 9i 7.61999987
corc811 -6.9345 -6.6545
c
c photon flux through OPD - check for FMESH tally 874
rmesh821:p flux
cora821 -0.27875 -0.03875
corb821 7.61999936 9i 7.61999987
corc821 -6.9345 -6.6545
c
c neutron energy deposition in OPD
rmesh831:n pedep
cora831 -0.27875 -0.03875
corb831 7.61999936 9i 7.61999987
corc831 -6.9345 -6.6545
c
c neutron dose delivered to OPD (rad)
rmesh841:n pedep
cora841 -0.27875 -0.03875
corb841 7.61999936 9i 7.61999987
corc841 -6.9345 -6.6545
c
c photon energy deposition in OPD
rmesh851:p pedep
cora851 -0.27875 -0.03875
corb851 7.61999936 9i 7.61999987
corc851 -6.9345 -6.6545
c
c photon dose delivered to OPD (rad)
rmesh861:p pedep
cora861 -0.27875 -0.03875
corb861 7.61999936 9i 7.61999987
corc861 -6.9345 -6.6545
c
c direct measurement of neutron dose delivered to OPD (rem/hr)
rmesh871:n dose
cora871 -0.27875 -0.03875
corb871 7.61999936 9i 7.61999987
corc871 -6.9345 -6.6545
c
c direct measurement of photon dose delivered to OPD (rem/hr)
rmesh881:p dose
```

```
cora881 -0.27875 -0.03875
corb881 7.61999936 9i 7.61999987
corc881 -6.9345 -6.6545
c
endmd
c
c Mesh tally multipliers
fm811 13.9018 9 444 $ converts flux tally to DPA for neutrons
fm841 1.602e-8 9 -1 -4 $ converts energy deposition to dose for neutrons (rad)
fm861 1.602e-8 9 -5 -6 $ converts energy deposition to dose for photons (rad)
c
c
c                          PROBLEM TERMINATION SPECIFICATIONS
c
nps 1e9
c in 20 hour run: 8.57e12 neutrons, 4.91601e12 gammas
```

APPENDIX B

SAMPLE NJOY INPUT

NJOY inputs were consistent between materials; the only major differences between them were in the `MAT` numbers used to refer to silicon, carbon, hydrogen, and sulfur isotopes. The following NJOY input file was used to develop neutron damage cross-section and photon kerma heating factor libraries for $^{28}_{14}$Si at room temperature (293.6 K).

```
moder
20 -21 /
reconr
-21 -22 /
'pendf tape for si-28 from endf/b-vii tape '
1425 2/
.001/
'14-Si-28 from ENDF/B-VII'/
'processed using NJOY'/
0/
broadr
-21 -22 -23
1425 1/
.001/
293.6
0/
heatr
-21 -23 -24/
1425 2/
443 444/
gaminr
-21 -23 0 -25
1425 7 3 4 0
'24 group photon library'/
-1/
0/
acer
-21 -24 0 31 32
1 0 1 .25/
'14-si-28 at 293.6 K from endf/b-vii'/
1425 293.6/
0/
/
acer
-21 -25 0 33 34
1 0 1 .25/
'14-si-28 at 293.6 K from endf/b-vii'/
1425 293.6/
0/
/
acer
```

```
42 0 31 35 36 37
43 7 1 2/
44 '14-si-28 from endf/b-vii neutrons'/
45 acer
46 0 33 38 39 40
47 7 1 2/
48 '14-si-28 from endf/b-vii photons'/
49 viewr
50 35 41/
51 viewr
52 38 42/
53 stop
```

REFERENCES

[1] G. F. Knoll, *Radiation Detection and Measurement*, 4th. John Wiley & Sons, Inc., 2011.

[2] R. Wunstorf, "Radiation hardness of silicon detectors: Current status," *IEEE Trans. on Nucl. Sci.*, vol. 44, pp. 806–814, 3 1997.

[3] G. Lindström, "Radiation damage in silicon detectors," *Nucl. Instr. and Meth. A*, vol. 512, pp. 30–43, 1-2 2003.

[4] S. Bates *et al.*, "Pion-induced damage in silicon detectors," *Nucl. Instr. and Meth. A*, vol. 379, pp. 116–123, 1 1996.

[5] R. Wunstorf, "Ph.D Thesis," PhD thesis, Universität Hamburg, 1992.

[6] G. Casse, "Radiation hardness of p-type silicon detectors," *Nucl. Instr. and Meth. A*, vol. 612, pp. 464–469, 3 2010.

[7] Y. Qiang *et al.*, "Radiation hardness tests of SiPMs for the JLab Hall D Barrel calorimeter," *Nucl. Instr. and Meth. A*, vol. 698, pp. 234–241, 2013.

[8] D. Žontar *et al.*, "Time development and flux dependence of neutron-irradiation induced effects in silicon pad detectors," *Nucl. Instr. and Meth. A*, vol. 426, pp. 51–55, 1 1999.

[9] T. M. Khan, "Organic semiconductor bulk heterojunction diodes with low dark current for photovoltaic, photodetection, and scintillator-free ionizing radiation detection applications," PhD thesis, Georgia Institute of Technology, 2016.

[10] F. Pelayo García de Arquer *et al.*, "Solution-processed semiconductors for next-generation photodetectors," *Nature Reviews Materials*, vol. 2, pp. 1–16, 2017.

[11] N. Sariciftci *et al.*, "Semiconducting polymer-buckminsterfullerene heterojunctions: Diodes, photodiodes, and photovoltaic cells," *Appl. Phys. Lett.*, vol. 62, pp. 585–587, 6 1993.

[12] S. E. Shaheen *et al.*, "2.5% efficient organic plastic solar cells," *Appl. Phys. Lett.*, vol. 78, pp. 841–843, 6 2001.

[13] J. You *et al.*, "A polymer tandem solar cell with 10.6% power conversion efficiency," *Nature Communications*, vol. 4, pp. 1–10, 2013.

[14] X. Gong *et al.*, "High-detectivity polymer photodetectors with spectral response from 300 nm to 1450 nm," *Science*, vol. 325, pp. 1665–1667, 5948 2009.

[15] A. Neuhold *et al.*, "X-ray radiation damage of organic semiconductor thin films during grazing incidence diffraction experiments," *Nucl. Instr. and Meth. B*, vol. 284, pp. 64–68, 2012.

[16] P. E. Laibinis *et al.*, "X-ray damage to CF_3CO_2-terminated organic monolayers on Si/Au: Principal effect of electrons," *Science*, vol. 254, pp. 981–983, 5034 1991.

[17] K. Heister *et al.*, "Characterization of x-ray induced damage in alkanethiolate monolayers by high-resolution photoelectron spectroscopy," *Am. Chem. Soc.*, vol. 17, pp. 8–11, 1 2001.

[18] R. Street, J. Northrup, and B. Krusor, "Radiation induced recombination centers in organic solar cells," *Phys. Rev. B*, vol. 85, pp. 1–13, 2012.

[19] S. Mouatassim *et al.*, "The light yield response of NE213 organic scintillators to charged particles resulting from neutron interactions," *Nucl. Instr. Meth. A*, vol. 359, pp. 530–536, 3 1995.

[20] J. Birks, *The Theory and Practice of Scintillation Counting*. Pergamon Press, 1964.

[21] G Dearnaley and D. Northrop, *Semiconductor Counters for Nuclear Radiations*. E. & F. N. Spon Limited, 1964.

[22] T. Graham Solomons and C. B. Fryhle, *Organic Chemistry*, 10th. John Wiley & Sons, Inc., 2011.

[23] S. Yoo, B. Domercq, and B. Kippelen, "Efficient thin-film organic solar cells based on pentacene/C_{60} heterojunctions," *Appl. Phys. Lett.*, vol. 85, pp. 5427–5429, 22 2004.

[24] N. D. Treat and M. L. Chabinyc, "Phase separation in bulk heterojunctions of semiconducting polymers and fullerenes for photovoltaics," *Annu. Rev. Phys. Chem.*, vol. 65, pp. 59–81, 1 2014.

[25] G Lindström, M Ahmed, S Albergo, P Allport, D Anderson, L Andricek, M. Angarano, V Augelli, N Bacchetta, P Bartalini, *et al.*, "Radiation hard silicon detectorsdevelopments by the RD48 (ROSE) collaboration," *Nuclear Instruments and Methods in Physics Research Section A: Accelerators, Spectrometers, Detectors and Associated Equipment*, vol. 466, no. 2, pp. 308–326, 2001.

[26] M. Moll, E Fretwurst, G Lindström, *et al.*, "Leakage current of hadron irradiated silicon detectors - material dependence," *Nuclear Instruments and Methods in Physics*

Research Section A: Accelerators, Spectrometers, Detectors and Associated Equipment, vol. 426, no. 1, pp. 87–93, 1999.

[27] J Armstrong *et al.*, "MCNP Users Manual Code Version 6.2," LA-UR-17-29981, CJ Werner ed., Los Alamos National Laboratory, Tech. Rep., 2017.

[28] "Reference neutron radiations - part 1: Characteristics and methods of production," International Organization for Standardization, Geneva, CH, Standard, 2001.

[29] D. Thomas *et al.*, "Revision of ISO 8529 - reference neutron radiations," *Radiation Protection Dosimetry*, pp. 1–4, 2017.

[30] Z. Liu, J. Chen, P. Zhu, Y. Li, and G. Zhang, "The 4.438 MeV gamma to neutron ratio for the Am-Be neutron source," *Applied Radiation and Isotopes*, vol. 65, no. 12, pp. 1318–1321, 2007.

[31] R. J. McConn *et al.*, "Compendium of material composition data for radiation transport modeling - revision 1," Pacific Northwest National Laboratory (PNNL), Richland, WA (US), Tech. Rep., 2011.

[32] R. E. MacFarlane, D. W. Muir, and F. Mann, "Radiation damage calculations with NJOY," *Journal of Nuclear Materials*, vol. 123, pp. 1041–1046, 1 1984.

[33] E. A. Read and C. R. E. de Oliveira, "A functional method for estimating DPA tallies in Monte Carlo calculations of light water reactors," in *Proceedings of 2011 International Conference on Mathematics and Computational Methods Applied to Nuclear Science and Engineering*, American Nuclear Society (Latin American Section), 2011.

[34] J. Lefèvre, J.-M. Costantini, S. Esnouf, and G. Petite, "Silicon threshold displacement energy determined by photoluminescence in electron-irradiated cubic silicon carbide," *Journal of Applied Physics*, vol. 105, no. 2, pp. 1–6, 2009.

[35] G. Montet, "Threshold energy for the displacement of atoms in graphite," *Carbon*, vol. 5, no. 1, pp. 19–23, 1967.

[36] F. Bryant and A. Cox, "Experimental and calculated atomic displacement threshold energies for binary semiconductors," *Proceedings of the Royal Society of London. A. Mathematical and Physical Sciences*, vol. 310, no. 1502, pp. 319–339, 1969.

[37] R. E. MacFarlane and A. Kahler, "Methods for processing ENDF/B-VII with NJOY," *Nuclear Data Sheets*, vol. 111, pp. 2739–2890, 12 2010.

[38] R. MacFarlane, D. W. Muir, R. Boicourt, A. C. Kahler III, and J. L. Conlin, "The NJOY Nuclear Data Processing System, Version 2016," Los Alamos National Lab, Tech. Rep., 2017, pp. 43–627.

[39] H. R. V. Carrillo, "Geometrical efficiency for a parallel disk source and detector," *Nuclear Instruments and Methods in Physics Research Section A: Accelerators, Spectrometers, Detectors and Associated Equipment*, vol. 371, no. 3, pp. 535–537, 1996.

[40] J. A. Favorite, "The solid angle (geometry factor) for a spherical surface source and an arbitrary detector aperture," *Nuclear Instruments and Methods in Physics Research Section A: Accelerators, Spectrometers, Detectors and Associated Equipment*, vol. 813, pp. 29–35, 2016.

[41] X-5 Monte Carlo Team, "MCNP - A General Monte Carlo N-Particle Transport Code, Version 5 Vol. I: Overview and Theory," *LA-UR-03-1987*, vol. 1, pp. 108–166, 2003.

[42] Z. Li and H. Kraner, "Fast neutron radiation damage effects on high resistivity silicon junction detectors," *Journal of electronic materials*, vol. 21, no. 7, pp. 701–705, 1992.

[43] J. Srour and D. Lo, "Universal damage factor for radiation-induced dark current in silicon devices," *IEEE Transactions on Nuclear Science*, vol. 47, no. 6, pp. 2451–2459, 2000.